

NASA Public Access

Author manuscript

IEEE J Sel Top Appl Earth Obs Remote Sens. Author manuscript; available in PMC 2017 September 13.

Published in final edited form as:

IEEE J Sel Top Appl Earth Obs Remote Sens. 2017 May ; 10(5): 2307–2320. doi:10.1109/JSTARS.2016.2629418.

Polar Applications of Spaceborne Scatterometers

David G. Long [Fellow, IEEE]

Electrical and Computer Engineering, Brigham Young University, Provo, UT 84602 USA
(long@ee.byu.edu)

Abstract

Wind scatterometers were originally developed for observation of near-surface winds over the ocean. They retrieve wind indirectly by measuring the normalized radar cross section (σ^0) of the surface, and estimating the wind via a geophysical model function relating σ^0 to the vector wind. The σ^0 measurements have proven to be remarkably capable in studies of the polar regions where they can map snow cover; detect the freeze/thaw state of forest, tundra, and ice; map and classify sea ice; and track icebergs. Further, a long time series of scatterometer σ^0 observations is available to support climate studies. In addition to fundamental scientific research, scatterometer data are operationally used for sea-ice mapping to support navigation. Scatterometers are, thus, invaluable tools for monitoring the polar regions. In this paper, a brief review of some of the polar applications of spaceborne wind scatterometer data is provided. The paper considers both C-band and Ku-band scatterometers, and the relative merits of fan-beam and pencil-beam scatterometers in polar remote sensing are discussed.

Keywords

Advanced scatterometer (ASCAT); backscatter; Earth remote sensing satellite (ERS); firn; freeze/thaw; ice; NASA scatterometer (NSCAT); OceanSat; polar; QuikSCAT; Seasat scatterometer (SASS); SeaWinds; scatterometer; snow

I. Introduction

Microwave wind scatterometers measure the normalized radar cross section (σ^0) of the Earth's surface. They are designed for ocean observation where the near-surface wind speed and direction are estimated from the σ^0 measurements [1]. The σ^0 measurements have proven utility in studies of land, vegetation, and ice. The frequent, wide-area coverage of the polar regions by scatterometers is particularly well suited for polar observation, where the σ^0 measurements have been used for such purposes as: Mapping snow cover and the freeze/thaw state of land, snow, and ice surfaces; monitoring the extent and motion of sea ice; mapping and classifying sea-ice type; measuring snow accumulation; and tracking large icebergs. Standard scatterometer-derived products are produced by a number of agencies for both operational and research purposes. The latter is facilitated by the long record of wind scatterometer σ^0 observations that begins in 1978 and has continued, with some gaps, to the

present. This data represent the longest record of active microwave observations of the Earth available.

The polar regions play an essential role in regulating global climate. Sea ice acts as an insulating layer between the ocean and atmosphere and increases the albedo of the polar oceans during winter that affects global atmospheric circulation [2]. Large continental ice sheets covering Greenland and Antarctica, as well as smaller ice sheets on islands, influence planetary albedo and provide freshwater input to ocean circulation [3]; such ice sheets are sensitive indicators of global climate change [4]. Permafrost regions are important methane reservoirs with the potential for releasing large amounts of methane with increasing temperatures [5], and extensive regions of tundra and boreal forest are important carbon sources and sinks that are active during the summer [6].

The unique capabilities and long record of scatterometer data provide a tool for the study of climate and conditions in the polar regions. In this paper, we briefly review the use of spaceborne scatterometer data in the polar regions with consideration of both operational and research applications. The paper is organized as follows: After some brief background in Section II and an introduction to electromagnetic scattering from snow and ice in Section III, scatterometer applications for sea-ice mapping are considered in Section IV, followed by a discussion of glacial ice applications in Section V. Iceberg tracking is considered in Section VI. Finally, a summary conclusion is provided in Section VII.

II. Background

From σ^0 measurements, wind scatterometers retrieve the near-surface wind over the ocean with the aid of a geophysical model function that relates the σ^0 to wind speed and direction. To resolve potential wind directional ambiguities, the wind scatterometer makes multiple σ^0 measurements of the same location on the Earth from several different azimuth angles, incidence angles, and/or polarizations. A good summary of scatterometer design and the theory of scatterometer wind retrieval is provided in [1].

Two primary scatterometer architectures have been flown in space: Fan beam and pencil beam, see Table I. Examples of fanbeam scatterometers are the Ku-band National Aeronautics and Space Administration (NASA) Seasat scatterometer (SASS) [7], which operated for three months in 1978; Ku-band NASA scatterometer (NSCAT) [8], which operated for nine months in 1996–1997; the two C-band European Space Agency (ESA) Earth remote sensing satellite (ERS-1 & ERS-2) scatterometers [9], which operated from 1992 to 2002; the C-band ESA advanced scatterometers (ASCAT-1 & ASCAT-2) [10], which began operation in 2007 and continue to operate; and the Chinese HY-2A scatterometer [11], which was launched in 2011. Examples of pencil-beam scatterometers include the Ku-band NASA SeaWinds [12], [13] series (QuikSCAT 1999–present; SeaWinds on ADEOS-II 2003; RapidScat 2014–present); the Ku-band Indian Space Research Organization (ISRO) OceanSat-2 scatterometer (OSCAT) [14], which operated from 2009 to 2014; and the recently launched ISRO OSCAT-2 on SCATSat-1 (2016–). Fan-beam scatterometers use multiple antennas at different azimuth angles to provide a fixed number of multiple azimuth looks. Measurements are collected over a range of incidence angles,

typically $\sim 20^\circ$ to 60° . Pencilbeam scatterometers employ a rotating antenna to collect measurements at two different incidence angles and a wide diversity of azimuth angles. Both systems have advantages and disadvantages for polar studies. The diversity of incidence angles available from fan-beam systems enables study of scattering mechanisms but has variable sensitivity across the swath; pencil-beam systems have finer azimuth sampling and wider coverage but fixed incidence angles. With their wide swaths, both architectures provide frequent, global observations. Their polar orbits typically provide twice daily sampling of the polar regions, with the exception of RapidScat whose orbit does not permit polar coverage.

The other key division in historic scatterometers is the operational frequency: Ku-band (13–14 GHz or ~ 2.1 cm) or C-band (5.4 GHz or ~ 5.4 cm). All ESA scatterometers have operated at C-band, whereas NASA and ISRO scatterometers have operated at Ku-band. The shorter wavelength provides greater ice/water contrast but reduced penetration and greater atmospheric sensitivity. Note that all past and present C-band scatterometers have operated at vertical polarization (VV), whereas all Ku-band scatterometers have included both VV and horizontal polarization (HH). A diversity of polarizations can provide additional information when discriminating surface characteristics. All wind scatterometers to date have been real-aperture systems.

To illustrate some of the information present in scatterometer data, Fig. 1 provides false-color images of Greenland and Antarctica created from combined dual-polarization QuikSCAT and single-polarization ASCAT data for a one-day period (day 217) in 2008. As discussed in detail later, the midsummer Greenland image in panel (a) illustrates the melt detection capability of these scatterometers. The dry snow central region has high backscatter due to volume scattering, and is surrounded by a band of lower backscatter that corresponds to the melt region. Fine details of the Antarctic ice sheet and sea-ice edge are revealed in panel (b) where variations in backscatter in sea ice are apparent in the Weddell Sea in the upper half of the image. Frequent observations of the backscatter in these areas enable monitoring of the melt region and tracking of sea-ice motion and conditions.

Since scatterometers use active radar sensing, the spatial resolution of scatterometer observations is higher than that of passive radiometer sensors [1], particularly when coupled with advanced reconstruction techniques that exploit the dense oversampling [15]. A scatterometer transmits a signal toward the Earth's surface and measures the return echo power. The scatterometer-observed backscatter is related to the antenna pattern and signal processor response via the integral form of the radar equation [1]. Ignoring atmospheric effects, the measured radar echo power P_r for a particular measurement is given by

$$P_r = \frac{P_T \lambda}{(4\pi)^3} \iint \frac{G_a^2(x, y) G_p(x, y) \sigma^o(x, y, \theta, \phi, t, p)}{R^4(x, y)} dx dy + \text{noise}. \quad (1)$$

where P_T is the transmit power, λ is the radar wavelength, $G_a(x, y)$ is the effective two-way antenna gain at the surface, $G_p(x, y)$ is the processor gain at x, y , and $R(x, y)$ is the slant range from the radar to the surface. The surface $\sigma^o(x, y, \theta, \phi, t, p)$ is a function of location x ,

y , incidence angle θ , azimuth angle ϕ , time t , and polarization p (VV or HH). Both θ and ϕ are functions of x and y , respectively, but vary only slightly for a single measurement. The integration is over the region of nonnegligible $G_a G_p$. By assuming σ^o is constant over the footprint, the surface σ^o at a given time is estimated from P_r and a separate estimate P_n of the noise-only power using

$$\sigma^o = \frac{P_r - P_n}{X} \quad (2)$$

where X is

$$X = \frac{(4\pi)^3}{P_T \lambda} [\iint \text{SFR}(x, y) dx dy]^{-1} \quad (3)$$

with the spatial response function SRF given by

$$\text{SRF}(x, y) = \frac{G_a^2(x, y) G_p(x, y)}{R^4(x, y)}. \quad (4)$$

For higher spatial resolution σ^o estimation, σ^o is assumed to vary over the footprint, and the SRF is used to reconstruct the surface σ^o field [16]. One reconstruction method is the scatterometer image reconstruction (SIR) algorithm [15], [17]–[19]. SIR uses signal reconstruction techniques to estimate σ^o on a fine-resolution grid, resulting in high-resolution backscatter images. SIR is also used with radiometer data to produce brightness temperature images [20], [21].

III. Scattering in the Polar Regions

The polar regions are dominated by glacial-ice covered surfaces, sea ice, and open ocean. They also include extensive regions of tundra, permafrost, and boreal forest. Over open water, scatterometers provide wind and wave observations that support studies of ocean currents, freshwater flux, waves, and wind/ice interaction [3], [22]–[24]. Recent algorithm improvements enable wind retrieval closer to ice and land and at higher resolution than ever before [25]–[28].

Scatterometer measurements have proven useful for monitoring freeze/thaw in the boreal regions in a number of studies [29]–[32]. The techniques used for determining melt are similar to those employed for glacial ice melt detection, so in this paper, we focus on snow and ice. A good introduction to the physics of radar backscatter from snow and ice is provided in [1]. Here, we review a few key points, which are supplemented in later sections.

For wind measurement over the ocean, the scatterometer relies on surface Bragg scattering from wind-generated waves [1]. Backscattering of microwave signals from snow and ice depends on roughness geometry and electrical properties, which in turn depends on the

physical characteristics of the snow and ice. Such scattering can be a mixture of volume and surface scattering [1]. For example, the presence of liquid water in snow dramatically changes its permittivity and thus its microwave scattering signature. This change provides an effective way of monitoring changes that result from melting and snow metamorphosis.

During winter, microwave signals can penetrate snow and ice and scatter off inhomogeneities, such as snow and ice layers and brine and air pockets in sea ice [33], [34]. Volume scattering from these and individual ice crystals creates a generally high backscatter dependent on geophysical conditions [1]. Note that the incidence angle dependence of σ^0 over the ocean is generally much steeper than over ice, though water-covered ice may have similar σ^0 and incidence angle dependence. The large difference in dielectric permittivity between seawater and sea ice aids in discriminating between open water (which may be wind roughened) and sea ice by using scatterometer backscatter measurements [33]. The water/sea ice contrast tends to be greatest at Ku-band.

Newly formed sea ice tends to be thin and often saline. As sea ice ages, it becomes thicker, rougher, and less saline, properties that tend to increase its backscatter compared to new ice [1]. The resulting backscatter contrast between first-year and multiyear ice enables accurate scatterometer classification of sea ice by age, especially at Ku-band, at which the contrast is much more pronounced than at C-band. Melting conditions during the summer increase the liquid water content of sea ice and thereby increase its dielectric permittivity. Melting thus tends to suppress the contrast between first-year and multiyear ice, and between sea-ice and wind-roughened open water. During the period of advanced surface melt in late summer (August and September in the Arctic), scatterometer ice age discrimination becomes impractical. However, sea-ice coverage mapping is still possible, especially since the variability and directional dependence of ocean winds creates high-variance backscatter over the ocean that contrasts with the generally smaller variance of backscatter from sea ice [25], [35], [36].

This is an advantage over radiometer measurements that also have difficulty mapping sea ice extent during summer. However, there is a longer, continuous dataset of radiometer measurements that also provide estimates of the percentage of sea-ice cover (sea-ice concentration) within each pixel. In contrast, scatterometer measurements have limited concentration capability [37] and suffer from a disjoint time series so radiometers continue to be considered the primary source for sea-ice mapping.

During summer, the principal parameter affecting the scatterometer backscatter response of the ice sheet is the appearance of liquid water in areas experiencing surface melt. The liquid water at the surface changes the scattering mechanism from volume scattering to surface scattering (see Fig. 2). This change produces lower backscatter. Thus, summer melt can be identified by large decreases in σ^0 . Refreezing returns the scattering to include volume scattering. The general backscatter behavior with melt is similar at C- and Ku-band.

Snow backscatter melt/freeze effects are illustrated for a glacial ice sheet in Fig. 3. Note that during the winter, indicated in gray, σ^0 (generally) gradually decreases (drops) due to snow accumulation attenuating buried volume scatters. In summer, rising temperatures lead to the

formation of moisture in the snow, producing deep drops in σ^o . Refreezing of melt water that has percolated into the firm, leads to the formation of buried ice features. These can increase the backscatter to greater than prior to the melt. This is readily apparent in 2001 and 2002. This effect tends to saturate as suggested by the smaller increase in 2003 after an equally large melt event.

Compared to synthetic aperture radar (SAR) systems, scatterometers provide more frequent coverage, albeit at lower resolution. Scatterometer measurements also provide spatial context for the higher resolution, but narrower swath SAR observations that are typically made at smaller incidence angles than scatterometer measurements. Measurements of the radar backscatter coefficient over a broad range of incidence angles can enable the scattering mechanism to be more readily determined and can aid in the estimation of ice characteristics [38]. Fan-beam scatterometers provide measurements over a range of incidence angles, something not possible with pencil-beam systems.

For comparison of measurements made at different incidence angles, it is often useful to parameterize the dependence of σ^o on incidence angle. Over a limited incidence angle range—say 20° to 60° , the range of incidence angles used by fan-beam scatterometers— σ^o (in dB) can be approximately expressed as a linear function of incidence angle θ

$$\sigma_{\text{dB}}^o(\theta) = \mathcal{A} + \mathcal{B}(\theta - \theta_{\text{ref}}) \quad (5)$$

where \mathcal{A} and \mathcal{B} are functions of surface characteristics, azimuth angle, and polarization. Typically $\theta_{\text{ref}} = 40^\circ$ (midswath). Note that \mathcal{A} is the σ^o value at θ_{ref} , i.e., $\mathcal{A} = \sigma_{\text{dB}}^o(40^\circ)$, while \mathcal{B} describes the average dependence of σ^o on θ in dB/deg. This model is primarily used for fan-beam scatterometer measurements. A popular alternate incidence angle model is given by

$$\gamma^o(\theta) = \sigma^o(\theta) / \cos \theta \quad (6)$$

where γ^o and σ^o are not in dB, but rather are linear values. When expressed in dB the model becomes

$$\gamma_{\text{dB}}^o(\theta) = \sigma_{\text{dB}}^o(\theta) - (10 \ln 10) \ln \cos \theta. \quad (7)$$

Note that $\gamma_{\text{dB}}^o(\theta)$ does not remove the incidence angle dependence of σ^o unless the target $\gamma_{\text{dB}}^o(\theta)$ has exactly a $\ln \cos \theta$ dependence that only occurs for the roughest surfaces.

Both the linear-in-dB and γ^o models have their merits and limitations. The γ^o model works well for very rough surfaces but the underlying $1/\cos \theta$ scale factor does not describe the σ^o versus θ rolloff characteristics of more specular surfaces [1]. For general scattering that consists of a combination of specular and rough scattering, it can be difficult to provide a consistent physical interpretation for γ^o . The γ^o model has the advantage of having only one

value to estimate (γ^o), whereas the linear-in-dB model has two, \mathcal{A} and \mathcal{B} . (We note that higher order polynomials models for σ^o versus incidence angle have even more parameters.) Although two parameters must be estimated for the linear-in-dB model, the value of \mathcal{B} provides additional information on the scattering mechanism, i.e., the \mathcal{B} values can be useful for discriminating surface from volume scattering [39]. The \mathcal{A} value has a physical interpretation as the value of σ^o (in dB) at the reference incidence angle. However, the linear-in-dB model is most accurate only near the reference incidence angle. As an illustration, Fig. 4 compares C-band images of γ^o with \mathcal{A} and \mathcal{B} images for a day in midwinter in the Northern Hemisphere. Note the generally similar appearance of the γ^o and \mathcal{A} images, though the γ^o image has a slightly higher dynamic range. The \mathcal{B} values provide some discrimination ability for multiyear versus first-year sea ice, as well as for melt conditions.

IV. Sea-Ice Mapping

Sea-ice cover in the polar regions is a critical input parameter to global climate models. The location of the sea-ice edge is also needed for accurate retrieval of ocean wind velocities from scatterometer measurements close to the sea ice [25]. Scatterometer data are well suited for sea-ice mapping because of the generally high backscatter contrast between sea-ice and open ocean, the rapid repeat coverage of the scatterometer in the polar regions, and low sensitivity to confounding atmospheric effects. In contrast, radiometer measurements provide coarser resolution and have high sensitivity to atmospheric effects and temperature. Scatterometer-derived ice products can also be higher resolution due to the finer resolution of the scatterometer measurements.

In the following sections, several applications of scatterometer data for sea mapping are considered, including ice-extent (sea-ice edge) mapping, sea-ice classification and ice age discrimination, sea-ice motion tracking, and melt onset. Many of these are operationally produced in support of navigation and weather forecasting [37], [40], [41].

A. Sea Ice Extent Mapping

While capable of independently determining the ice edge, scatterometer data complement passive microwave observations of the ice margin. Driven by wind and ocean currents, the scatterometer-observed sea-ice margin has been observed to move as much as 50 km in one day [42]. A number of investigators have developed algorithms for discriminating between sea ice and open ocean by using only scatterometer data [36], [43]–[48]. Scatterometer-derived ice margins provide an independent data source of evaluating the variability of ice coverage [49], [50] compared to radiometers.

The essential idea in mapping sea ice is to create images of \mathcal{A} and \mathcal{B} or γ^o and ancillary variables, such as the backscatter variance or the maximum fore/aft beam difference (d), as seen in Fig. 5. Single- or multivariate histograms of the parameters are computed to determine the mean and variance of the ocean and ice observations. These parameters are then used to classify each image pixel [1], sometimes with the aid of a prior [47] or in a full Bayesian detection approach [51]. Postclassification image processing and comparison with previous day images reduce classification errors [44].

A comparison of the seasonal area of Antarctic sea-ice extent computed from Ku-band scatterometer data by using the Remund–Long algorithm [36] and concentration-thresholded radiometer data suggests that there are seasonal biases in the two ice edges. The biases are apparent in Fig. 6. The general trends for both sensor types (active and passive) are very similar during the annual melt cycle. The edges differ the most during the ice retreat and advance phases. During ice retreat, the scatterometer-estimated ice extent is generally somewhat greater than the 30% ice concentration extent derived from special sensor microwave/imager (SSM/I), while during the ice growth phase the SSM/I ice extent is generally greater than the radiometer edge [37], [45], [54]. Similar trends are observed in C-band sea-ice maps. We suggest that during periods of rapid ice growth and retreat when the ice signature evolves rapidly, active (radars), and passive sensors have different sensitivities to diffuse edges, and that by coupling scatterometer and radiometer data, the accuracy of ice maps and ice classifications can be improved [55].

B. Sea-Ice Motion

Satellite observation of sea-ice motion aids in the monitoring of the ice dynamics for climate studies and ship routing applications. While Arctic and Antarctic sea ice exhibit different distributions of ice type and backscatter characteristics [56], sea-ice tracking applied to scatterometer data has been successful at both poles.

A number of researchers have developed algorithms to derive sea-ice motion from SAR images that have been applied to scatterometer backscatter data [37], [57]–[59]. In a particular approach, daily γ^o or σ^o images are constructed, and a wavelet transform applied. A template-matching algorithm is then employed to compare the current image to the previous image. Once matched, the mean velocity vector is then derived by dividing the relative displacement of key features over the image time interval. This procedure may be repeated over multiple scales to improve tracking performance [4], [58]. Optical flow techniques [59] provide an alternate approach to motion estimation, but are unfortunately more sensitive to temporal changes in the ice feature being tracked than correlation methods [59].

It has been noted that radiometer- and scatterometer-derived results are complementary. That is, that the scatterometer often provides good motion data when the radiometer is unable to. For example, combining the daily sea-ice drift results from NSCAT, SSM/I, and buoy data to create daily motion maps accurately identifies large-scale sea-ice dynamics [58].

As discussed in the Section IV-C, scatterometer-derived sea-ice motion, coupled with sea-ice classification, helps explain the observed loss in multiyear sea ice in the Arctic. This analysis is aided by cross correlation and feature-tracking Lagrangian algorithms that exploit the backscatter contrast between multi-year (MY) and first year (FY) sea ice. MY ice is sea ice that has survived the melt season, whereas FY ice has not passed through a summer season and thus has different physical and backscatter properties [60].

C. Sea Ice Classification

Because of the many types of sea ice and its dynamic nature, scattering from sea ice is very complicated [1]. Due to the metamorphic processes occurring over its history, MY ice is

typically relatively thick and has a very deformed surface with low salinity and low microwave signal absorption. The scattering is dominated by volume scattering, which produces a high σ^0 value with a low β value. FY ice can also be highly deformed with a rough surface due to ridging; however, it typically has higher salinity and microwave signal absorption. The resulting scattering is driven by surface scattering, which produces medium to high σ^0 and β values at Ku-band. Smooth FY ice has little deformity and is thinner. Its high salinity and microwave absorption result in medium to low σ^0 values and low β values. The Nilas class is young, thin (typically <10 cm), smooth ice that forms in calm conditions usually in polynyas or open leads. It quickly evolves into rougher FY ice due to deformation by wave action and ridging. It has very low σ^0 and β values. With its higher σ^0 , MY ice can be mapped relative to FY ice due to the backscatter contrast that differs somewhat between the poles [56]. The FY/MY ice σ^0 contrast is frequency dependent, with Kuband having significantly higher contrast than C-band [61].

A large number of studies have been conducted to classify sea ice. Those using pencil-beam scatterometers have focused primarily on MY and FY ice classification [48], [62], [63], while others working with fan-beam systems discriminate additional ice types [4], [39], [43], [61], [64], [65]. Other researchers have employed additional sensors to aid in classification [66]–[69]. Most of these methods share the general approach of creating feature vectors with either fixed reference vectors, dynamically-selected reference vectors, or automated clustering techniques to classify the observed scattering characteristics for each pixel to a particular ice type [1].

Combining ice age classification (MY versus FY ice) with ice motion estimates, researchers [70]–[72] observed the decline of perennial sea-ice cover in the Arctic due to the advection of MY ice southward along the west coast of Greenland. The decline in MY ice thins the ice cap [73]. The scatterometer backscatter record has the potential to support a continuous 25 year record of sea-ice type. As a step in this direction, [63] created a 15-year Ku-band record from QuikSCAT and OSCAT (see Fig. 7). The decline in MY ice from 2002 to 2013 is apparent, but a significant recovery of MY ice coverage is observed in 2014. A full recovery is uncertain and it is unlikely that the 2014-retained MY ice is as thick as the MY ice a decade earlier.

D. Melt-Onset Mapping

Summer melting significantly affects the albedo of the polar oceans, that results in a positive warming feedback effect [74]. Monitoring the timing and areal extent of summer melting is thus of great interest in weather and climate studies. As previously noted, the σ^0 of snow and ice is particularly sensitive to the presence of liquid water. This melt sensitivity makes scatterometer σ^0 measurements an excellent tool for delineation of the freeze/thaw state of snow, sea ice [75], and glacial ice [4].

Moisture levels in the frozen snow cover are negligible during the winter months, so the snow layer is essentially transparent. As temperature increases in the spring and summer, and liquid water content of the snow increases, resulting in more forward scattering and decreased backscatter [76]. This temperature-driven backscatter change in snow has been

used to map snow and melt onset over the Arctic Ocean [30], [77]–[79], freshwater lakes [80], [81], and over land in northern Canada [30] and globally [82].

V. Glacial Ice

Glacial ice forms from accumulated snow. As previously noted, liquid water in the surface layer formed during the summer melt changes the dominant scattering mechanism from volume to surface scattering (see Fig. 2), which results in significant decreases in the σ^o of Greenland firn, often exceeding 15 dB [38], [83]. Thus, the extent of the summer melt can be delineated by areas that have large drops in σ^o . Typically melting ceases by late summer, with refreezing resulting in increased σ^o . Snow that accumulates on the surface during the winter causes attenuation of the scattering from prior melt features, resulting in a drop in σ^o related to the net accumulation [4], [84]–[87]. The value of \mathcal{A} or γ^o thus tends to reflect the melt history and accumulation of the study point.

In the following sections, some scatterometer applications for monitoring the Greenland and the Antarctic ice cover are briefly considered. These include melt and accumulation mapping.

A. Greenland Ice Sheet

The Greenland ice sheet can be conveniently divided into zones or “facies” within which near-surface snow, firn, and ice properties have unique characteristics, see Fig. 8 [88]. The geophysical boundaries are not always distinct, but are defined by the timing and expression of melt conditions. Referring to Fig. 9, at the lowest elevations, summer melting removes prior accumulation of snow to expose glacial ice. The so-called *firn line* delimits the upper margin of this zone from the saturated or “soaked” zone, which is the region in which the snow layer is completely water saturated. The upper limit of the saturated zone is called the *saturation line*. Above this line is the *percolation zone*, where meltwater drips into the snow and refreezes, creating buried ice features termed “ice lenses” or “ice glands.” Between this region and the limit of surface melt is the *dry snow line*, above which very little melting occurs. This area consists of annual layers of ice “wind slabs” separated by accumulated snow [38], [83]. These glacier facies are best discerned with measurements penetrating several meters into the snow and ice surface. Since they provide such penetration, the microwave frequencies used by scatterometers are well suited for snow and ice observation because σ^o is sensitive to both surface and subsurface characteristics [4], [69], [83], [84], [89]–[92].

Scattering from wet and saturated snow is related primarily to the surface geometry and the surface roughness at the scale of the wavelengths. Some success has been obtained in determining the “intensity” (i.e., the amount) of the melt by observing depth and diurnal variability of the backscatter [93], but further work is required to develop the technique.

In dry snow, C-band microwaves penetrate somewhat more effectively than Ku-band, with relatively smaller absorption scattering and absorption losses. This is evident in the changes in color of the snow and ice in Fig. 1, where the false color is related to the backscatter at each frequency. At Ku-band, microwaves are more effectively scattered by the snow grains

and thin ice layers, thereby resulting in larger Ku-band σ^o values in the dry snow zone, in the center of the Greenland. Multiple layers from annual accumulation complicate this when large-scale coherent structures, such as snow dunes or sastrugi are involved [94]. These features can introduce a wind-dependent azimuth variation to the backscatter not seen in sea ice. This “azimuth modulation” of the backscatter can be used to map the long-term average wind direction in Greenland [90] and Antarctica [94]–[97] at both C- and Ku-bands. The relationship between buried-layer azimuth scattering and snow-free “wind-glaze” regions in Antarctica is not well understood [97], [98].

Since it experiences no melting, the dry snow zone has relatively little variation in backscatter over a season. The precise value of σ^o (or \mathcal{A}) is related to the accumulation [38], [85]. The long-term consistency of scattering in the Greenland dry snow zone has led to its use in scatterometer cross calibration [99], though recently observed strong melts [100] raise concerns about the long-term viability of the dry snow zone for this purpose.

By evaluating σ^o time series to find σ^o drops associated with melt, a number of investigators have mapped key ice zones on Greenland by using daily-averaged backscatter from scatterometers with various algorithms [38], [83], [101]–[106]. Similar approaches have been successfully used to map snow facies and melting in Antarctica [92], [107] and in various ice caps [108], [109]. While details vary, the consistency of the results from the various studies confirm the utility of the scatterometer for ice facies mapping.

Exploiting multiple passes per day for the polar region, scatterometers can evaluate the intensity of snow melting by examining the variation in σ^o during the day [93]. Diurnal backscatter differences have been used by [87], [102], [110] to map melting in Greenland and Antarctica.

B. Antarctic Ice Shelves

Variations in snow accumulation are evident as scatterometer σ^o variations in the dry snow zone [85]. For example, the color variations in West Antarctica (the lower right quadrant of panel (b) of Fig. 1) are correlated with net accumulation. Localized accumulation is affected by local wind conditions than can create the huge “mega-dunes” that are visible near the right edge of panel (b) in Fig. 1.

Evidence of warming in the seas around Antarctica over the past few decades has raised concerns about the stability of the large ice shelves in that region, especially in light of the disintegration of the Larsen ice Shelf in two large events monitored by radar [4], [34], [111] as well as other ice shelf collapses. It has been suggested that protracted summer melts may have contributed to weakening of the ice shelves that lead to their eventual collapse [34]. Scatterometer melt maps have revealed some particularly intense summer melts on ice sheets that later collapsed, notably the Larsen and Wilkins ice shelves [112]. Existing ice shelves are experiencing both increased basal melting from a warming ocean [113], [114] and more intense surface melting from recent summer melt events.

VI. Iceberg Tracking

Forced by winds and currents, icebergs represent major hazards to navigation, but tabular icebergs are also critical to southern ocean biology via the transport of freshwater and nutrients [115]. Fertilization from these “biological islands” supports an extensive food chain from the smallest to the largest of organisms [116]. Tabular Antarctic icebergs are also useful proxies for studying the breakup of major ice shelves [117].

Large icebergs are visible in scatterometer data due to the high backscatter contrast between the glacial ice that makes up the iceberg and the ocean, see Fig. 1. From the data, daily iceberg positions can be derived under all lighting conditions and irrespective of clouds [118], [119]. The backscatter contrast is highest at Ku-band compared to C-band, which makes icebergs easier to track at Ku-band than at C-band. The wider coverage of pencil-beam scatterometers also aids in iceberg tracking. Unfortunately, during the summer surface melt and the formation of melt ponds on the iceberg’s surface can reduce the iceberg’s σ^0 and produce temporary loss of backscatter contrast with the backscatter of the ocean, particularly in strong wind conditions. The relatively coarse resolution of scatterometer measurements limits the size of icebergs that can be identified and tracked to greater than ~5 km at Ku-band and slightly larger at C-band [118].

Scatterometer data have been used operationally for tracking major Antarctic icebergs since shortly after the launch of QuikSCAT, when the first QuikSCAT σ^0 image (see Fig. 10) produced of Antarctica revealed the presence of iceberg B10A in the Drake passage in 1999. Previous to this, the location of this 65 nmi by 25 nmi, ~300 m thick iceberg had been unknown after four months of movement from its last known position north of Pine Island, Antarctica—a distance of several thousand kilometers [120]. Since B10A’s discovery icebergs positions have been regularly extracted from near real-time scatterometer data for each new sensor. Iceberg positions have been harvested from historic scatterometer datasets to provide a long climate series of large (>5–10 nmi largest dimension) iceberg positions that spans nearly 40 years.

Fig. 11 illustrates all Antarctic iceberg positions reported from scatterometer data spanning 1978 to June, 2016. Minimum iceberg size varies from ~5 to 15 km. Analysis of this data reveals that well over 95% of all Antarctic icebergs travel through the Weddell Sea, regardless of their origin [118]. Other important observations include the fact that icebergs tend to move slowly when surrounded by sea ice and faster in the open ocean. Some very large (>25 km) icebergs have been observed to travel 75 km in a day [118].

In addition to navigation hazard avoidance, iceberg position data have been used to guide ships to study icebergs and their environs [115], [116], validate iceberg positions derived from other sensors, such as altimeters [121] and acoustic arrays [122]–[124], and address iceberg-related climate questions [125]. Altimeters observe icebergs over very narrow tracks via iceberg height above the surrounding ocean [121], while acoustic methods rely on triangulation of noise generated by the iceberg due to internal stress and calving [123].

Fig. 12 shows a plot of the number of Antarctic icebergs being tracked by the U.S. National Ice Center (NIC) from 1978 to May 2016 compared with counts of icebergs derived

(separately) from different scatterometers. Note that the NIC under-counted icebergs prior to 1986 but later better matches the scatterometer counts, in part because they began using scatterometer data. The strong rise in the number of icebergs in multiple steps after 1999 is the result of major calving events from the Ross and Ronne ice shelves [125]. While the breakup of several major ice shelves [34], [117] has been related to warming conditions, the count of major icebergs appears to be more reflective of the historic timing of calving events than of modern warming [125]. Thinning of major ice shelves due to ocean warming may, however, increase the rate of calving in the future.

VII. Future Directions

The future of scatterometry is bright, with multiple missions in various stages of planning by the U.S., ESA, India, China, Japan, and Russia [126]. Future mission plans include single frequency C- or Ku-band sensors, as well as dual-band (C- and Ku-band) sensors. The latter will be able to directly exploit the backscatter differences of different snow and ice types to better classify ice and precipitation in a single pass. Ka-band wind scatterometers are also being investigated. The higher frequency operation should provide greater contrast between ocean, sea ice, and icebergs. It will enable tracking of smaller icebergs.

Future scatterometer systems will include polarimetric capability, such as that proposed for the C-band dual polarimetric wind scatterometer to be flown on the second generation meteorological operation satellite program (MetOp-SG) [127]. SAR studies have shown that polarimetric backscatter measurements are effective in extending the number of ice classes that can be differentiated [1], which suggests that polarimetric scatterometers will enable improved sea-ice classification and mapping. Further cross-polarization capability should improve the sensitivity to a wider range of melt conditions.

Larger antennas and/or higher frequency operation will provide higher intrinsic resolution. This will enable more accurate estimates of the sea-ice edge and possibly enable estimation of how diffuse the sea ice is at the edge, i.e., estimate sea-ice concentration. High resolution can also support better mapping of polynyas, and may be able to enable estimation of the vector wind over open water in leads and polynyas using specialized geophysical model functions. Finer resolution will enable more accurate tracking of smaller icebergs, and facilitate automated iceberg size measurement and orientation.

It is expected that scatterometry technology will continue to improve. For example, the development of a rotating beam SAR-scatterometer will enable both very high resolution and multiple azimuth observation for wind applications over ocean and sastrugi. Doppler scatterometers designed for both wind and current observation over the ocean, may be also able to directly measure sea-ice motion. Improved technology will also enhance the timeliness of the delivery of scatterometer products to end users. Higher power transmitters will improve the signal-to-noise ratio of the σ^0 measurements, reducing the uncertainty in derived products.

Continuing validation efforts for existing products will provide greater confidence in both science and operational products and wider adoption of them. Operationalization of research

products, such as scatterometer-derived sea-ice motion will provide operational users with improved ship routing tools.

VIII. Conclusion

This paper has briefly considered some of the polar applications of scatterometer backscatter measurements. Scatterometry is clearly a powerful and effective tool for polar observation. Among other applications, scatterometer data are used to map sea-ice extent, measure sea-ice motion, classify sea-ice type, monitor sea-ice and ice-sheet melt, quantify snow accumulation, and measure wind over Antarctica. In addition to its research utility, scatterometer data in the polar regions is routinely and operationally used for sea-ice monitoring and iceberg tracking. Given the importance of the polar regions in regulating global climate, continued monitoring of the polar regions is critical. Note that the real value for future scatterometer missions is to continue the now 30-year long climate record of scatterometer observations of the polar region. This climate record provides baseline for evaluating future changes in the polar regions, and continuing the observation will help us to better understand long-term changes in sea-ice and land-ice sheets.

IX. Scatterometer Data Availability

Operational scatterometer polar products from current scatterometers are available from various data centers including the National Oceanic and Atmospheric Administration (manati.star.nesdis.noaa.gov), the Royal Netherlands Meteorological Institute (www.knmi.nl), and the European Organisation for the Exploitation of Meteorological Satellites (EUMETSAT) (www.eumetsat.int), among others. Raw backscatter measurements are available from the Physical Oceanography Distributed Active Archive Center (PODAAC) (podaac.jpl.nasa.gov) and EUMETSAT. In addition the Brigham Young University Scatterometer Climate Pathfinder (SCP) project (www.scp.byu.edu) has an extensive set of compatible conventional resolution and enhanced-resolution scatterometer backscatter image datasets for the scatterometers mentioned in this paper. The SCP also maintains a database of daily scatterometer-derived iceberg positions spanning almost four decades as well as other scatterometer-derived products.

Acknowledgments

This work was completed at Brigham Young University Microwave Earth Remote Sensing Laboratory. Scatterometer data were obtained from the PODAAC at the Jet Propulsion Laboratory, Pasadena, CA, USA.

References

1. Ulaby, F., Long, DG. Microwave Radar and Radiometric Remote Sensing. Ann Arbor, MI, USA: Univ. Michigan Press; 2014.
2. Budikova D. Role of Arctic sea ice in global atmospheric circulation: a review. Global Planet. Change. 2009; 68:149–163.
3. Haine TWN, et al. Arctic freshwater export: Status, mechanisms, and prospects. Global Planet. Change. 2015; 125:13–35.
4. Long DG, Drinkwater MR. Cryosphere applications of nscat data. IEEE Trans. Geosci. Remote Sens. May; 1999 37(3):1671–1684. DOI: 10.1109/36.763287

5. Anthony KMW, Anthony P, Goose G, Chanton J. Geologic methane seeps along boundaries of Arctic permafrost thaw and melting glaciers. *Nature Geosci.* 2012; 5:419–426.
6. Pan Y, et al. A large and persistent carbon sink in the world's forests. *Science.* 2011; 333(6045): 988–993. [PubMed: 21764754]
7. Grantham WL, Bracalente E, Jones W. The Seasat-A satellite scatterometer. *IEEE J. Ocean. Eng.* Apr; 1977 OE-2(2):200–206.
8. Naderi F, Freilich MH, Long DG. Spaceborne radar measurement of wind velocity over the ocean—An overview of the NSCAT Scatterometer system. *Proc. IEEE.* Jun; 1991 79(6):850–866. DOI: 10.1109/5.90163
9. Attema EP. The active microwave instrument on-board the ERS-1 satellite. *Proc. IEEE.* Jun; 1991 79(6):791–799.
10. Figa-Saldaa J, Wilson JJW, Attema E, Gelsthorpe R, Drinkwater MR, Stoffelen A. The Advanced Scatterometer (ASCAT) on the meteorological operational (MetOp) platform: A follow on for European wind scatterometers. *Can. J. Remote Sens.* 2002; 23(3):404–412.
11. Yang X, li X, Yu Y, Li Z. Validation of sea surface wind vector retrieval from China's HY-2A scatterometer. *Proc. IEEE Int. Geosci. Remote Sens. Symp.* 2013; :1250–1253. DOI: 10.1109/IGARSS.2013.6723007
12. Spencer MW, Wu C, Long DG. Improved resolution backscatter measurements with the SeaWinds pencil-beam scatterometer. *IEEE Trans. Geosci. Remote Sens.* Jan; 2000 38(1):89–104. DOI: 10.1109/36.823904
13. QuikSCAT Science Data Product Users's Manual, Jet Propulsion Laboratory document D-18053, Jet Propulsion Laboratory. Pasadena, CA, USA: 2001.
14. Padia K, Team SD. OceanSat-2 Scatterometer algorithms for sigma-0, processing and products format," in. *Proc. Adv. Image Process. Group, Signal Image Process. Area, Space Appl. Centre.* Apr.2010 :1–8.
15. Long DG. Comparison of SeaWinds backscatter imaging algorithms. *IEEE J. Sel. Topics Appl. Earth Observ. Remote Sens.* 2016 this issue.
16. Williams BA, Long DG. Reconstruction from aperture-filtered samples with application to scatterometer image reconstruction. *IEEE Trans. Geosci. Remote Sens.* May; 2011 49(5):1663–1676. DOI: 10.1109/TGRS.2010.2086063
17. Long DG, Hardin P, Whiting P. Resolution enhancement of spaceborne scatterometer data. *IEEE Trans. Geosci. Remote Sens.* May; 1993 31(3):700–715. DOI: 10.1109/36.225536
18. Early DS, Long DG. Image reconstruction and enhanced resolution imaging from irregular samples. *IEEE Trans. Geosci. Remote Sens.* Feb; 2001 39(2):291–302.
19. Lindsley R, Long DG. Enhanced-resolution reconstruction of ASCAT backscatter measurements. *IEEE Trans. Geosci. Remote Sens.* May; 2016 54(5):2589–2601. DOI: 10.1109/TGARS.2015.2503762
20. Long DG, Brodzik MJ. Optimum image formation for spaceborne microwave radiometer products. *IEEE Trans. Geosci. Remote Sens.* May; 2016 54(5):2763–2779. DOI: 10.1109/TGARS.2015.2505677
21. Long DG, Daum DL. Spatial resolution enhancement of SSM/I data. *IEEE Trans. Geosci. Remote Sens.* Mar; 1998 36(2):407–417.
22. Bogucki DJ, Drennan WM, Woods S, Gremes-Cordero S, Long DG, Mitchell C. Short surface waves in the Canadian Arctic in 2007 and 2008. *J. Geophys. Res.—Oceans.* 2013; 118:3712–3722. DOI: 10.1002/jgrc.20273
23. Steele M, Zhang J, Rothrock D, Stern H. The force balance of sea ice in a numerical model of the Arctic Ocean. *J. Geophys. Res.* 1997; 102(C9):21061–21079.
24. Kimura N, Wakatsuchi M. Relationship between sea-ice motion and geostrophic wind in the Northern Hemisphere. *Geophys. Res. Lett.* 2000; 27(22):3735–3738.
25. Hullinger WJ, Long DG. Mitigation of sea ice contamination in QuikSCAT wind retrieval. *IEEE Trans. Geosci. Remote Sens.* Apr; 2014 52(4):2149–2158. DOI: 10.1109/TGRS.2013.2258400
26. Owen MP, Long DG. Land contamination compensation for QuikSCAT near-coastal wind retrieval. *IEEE Trans. Geosci. Remote Sens.* Mar; 2009 47(3):839–850. DOI: 10.1109/TGRS.2008.2005633

27. Verhoef A, Portabella M, Stoffelen A. High-resolution ASCAT scatterometer winds near the coast. *IEEE Trans. Geosci. Remote Sens.* Jul; 2012 50(7):2481–2487.
28. Lindsley R, Long DG. Analysis and validation of high-resolution wind from ASCAT. *IEEE Trans. Geosci. Remote Sens.* Oct; 2016 54(10):5699–5711.
29. Bartsch A, Kidd RA, Wagner W, Bartalls Z. Temporal and spatial variability of the beginning and end of daily spring freeze/thaw cycles derived from scatterometer data. *Remote Sens. Environ.* 2007; 106(3):360–374. DOI: 10.1016/j.rse.2006.09.004
30. Brown R, Derksen C, Wang L. Assessment of spring snow cover duration variability over Northern Canada from satellite dataset. *Remote Sens. Environ.* 2007; 111:367–381.
31. Frolking S, McDonald KC, Kimball J, Way JB, Zimmermann R, Running SW. Using the space-borne NASA scatterometer (NSCAT) to determine the frozen and thawed seasons of a boreal landscape. *J. Geophys. Res.* 1999; 104:27895–27908.
32. Naeimi V, Paulik C, Bartsch A, Wagner W. ASCAT Surface State Flag (SSF): Extracting information on surface freeze/thaw conditions from backscatter data using an empirical threshold-analysis algorithm. *IEEE Trans. Geosci. Remote Sens.* Jul; 2012 50(7):2566–2582.
33. Bindshadler R. Monitoring ice sheet behaviour from space. *Rev. Geophys.* 1998; 36(1):79–104.
34. Rott H, Skvarca P, Nagler T. Rapid collapse of northern Larsen ice shelf, Antarctica. *Science.* 1996; 271:788–792.
35. Early DS, Long DG. Azimuthal modulation of C-band scatterometer sigma-0 over Southern Ocean sea ice. *IEEE Trans. Geosci. Remote Sens.* Sep; 1997 35(5):1201–1209. DOI: 10.1109/36.628787
36. Remund QP, Long DG. A decade of QuikSCAT scatterometer sea ice extent data. *IEEE Trans. Geosci. Remote Sens.* Jul; 2014 52(7):4281–4290. DOI: 10.1109/TGRS.2013.2281056
37. Haarpainter J, Spreen G. Use of enhanced-resolution QuikSCAT/SeaWinds data for operational ice services and climate research: Sea ice edge, type, concentration, and drift. *IEEE Trans. Geosci. Remote Sens.* Oct; 2007 45(10):131–1317.
38. Long DG, Drinkwater MR. Greenland ice-sheet surface properties observed by the Seasat-A Scatterometer at enhanced resolution. *J. Glaciology.* 1994; 40(135):213–230.
39. Remund QP, Long DG. Large-scale inverse Ku-band backscatter modeling of sea ice. *IEEE Trans. Geosci. Remote Sens.* Aug; 2003 41(8):1821–1832. DOI: 10.1109/TGRS.2003.813495
40. Shokr M, Agnew TA. Validation and potential applications of Environment Canada ice Concentration Extractor (ECICE) algorithm to Arctic ice by combining AMSR-E and QuikSCAT observations. *Remote Sens. Environ.* 2013; 128:315–332. DOI: 10.1016/j.rse.2012.10.016
41. Buehner M, Caya A, Carrieres T, Pogson L. Assimilation of SSMIS and ASCAT and the replacement of highly uncertain estimates in the environment Canada Regional ice Prediction System. *Q. J. R. Meteorol. Soc.* 2016; 142(695):562–573. pt. B.
42. Allen JR, Long DG. Microwave observations of daily Antarctic sea-ice edge expansion and contraction rates. *Geosci. Remote Sens. Lett.* 2006; 3(1):54–58. DOI: 10.1109/TGRS.2005.856710
43. Yueh SH, Kwok R, Lou S, Tsai W. Sea ice identification using dual-polarized Ku-Band scatterometer data. *IEEE Trans. Geosci. Remote Sens.* May; 1997 35(3):560–569.
44. Remund QP, Long DG. Sea ice extent mapping using Ku band scatterometer data. *J. Geophys. Res.* 1999; 104(C5):11515–11527. DOI: 10.1029/98JC02373
45. Haarpainter J, Tonboe RT, Long DG, VanWoert ML. Automatic detection and validity of the sea ice edge: An application of enhanced resolution QuikSCAT/SeaWinds data. *IEEE Trans. Geosci. Remote Sens.* Jul; 2004 42(7):1433–1443. DOI: 10.1109/TGRS.2004.828195
46. Gohin F, Cavanie A. A first try at identification of sea ice using the three beams of ERS-1. *Int. J. Remote Sens.* 1994; 15:1221–1228.
47. Anderson HS, Long DG. Sea ice mapping method for SeaWinds. *IEEE Trans. Geosci. Remote Sens.* Mar; 2005 43(3):647–657. DOI: 10.1109/TGRS.2004.842017
48. Li M, Zhao C, Zhao Y, Wang L, Shi Z. Polar sea ice monitoring using HY-2A scatterometer measurements. *Remote Sens. Art*; 2016 6(688)doi: 10.3390/rs8080688
49. Drinkwater MR, Lytle VI. ERS-1 radar and field-observed characteristics of autumn freeze-up in the Weddell Sea. *J. Geophys. Res.* 1997; 102(C6):12593–12608.

50. Drinkwater MR. Satellite microwave radar observations of climate-related sea-ice anomalies,” in. Bull. Amer. Meteorol. Soc., Proc. Workshop Polar Processes Global Climate. Nov 13–15.1997 : 115–118.
51. Rivas MB, Verspeek J, Verhoef A, Stoffelen A. Bayesian sea ice detection with the advanced scatterometer ASCAT. IEEE Trans. Geosci. Remote Sens. Jul; 2012 50(7):2646–2657.
52. Cavalieri D, et al. Aircraft active and passive microwave validation of sea ice concentration from the defense meteorological satellite program special sensor microwave imager. J. Geophys. Res. Dec; 1991 96(C12):21989–22008.
53. Cavalieri, D., Parkinson, C., Gloerson, P., Zwally, H. Sea ice Concentrations from Nimbus-7 SSMR and DMSP SSM/I-SSMIS Passive Microwave Data. Boulder, CO, USA: NASA DAAC at the National Snow and ice Data Center; 1996. (updated yearly)
54. Meier W, Stroeve J. Comparison of sea ice extent and ice edge location estimates from passive microwave and enhanced resolution scatterometer data. Ann. Glaciology. 2008; 48(1):65–70.
55. Yu P, Clausi DA, Howell SEL. Fusing AMSR-E and QuikSCAT imagery for improved sea ice recognition. IEEE Trans. Geosci. Remote Sens. Jul; 2009 47(7):1980–1990. DOI: 10.1109/TGRS.2009.2013632
56. Hosseinmostafa AR, Lytle VI, Jezek KC, Gogineni SP, Ackley SF, Moore RK. Comparison of radar backscatter from Antarctic and Arctic sea ice. J. Electromagn. Waves Appl. 1995; 9(3):421–438.
57. Haarpaintner J. Arctic-wide operational sea ice drift from enhanced-resolution QuikSCAT/SeaWinds scatterometry and its validation. IEEE Trans. Geosci. Remote Sens. Jan; 2006 44(1): 102–107.
58. Zhao Y, Liu AK, Long DG. Validation of sea ice motion from QuikSCAT with those from SSM/I and buoy. IEEE Trans. Geosci. Remote Sens. 2002; 40(6):1241–1246. DOI: 10.1109/TGRS.2002.800442
59. Gutierrez S, Long DG. Application of optical flow and scale space methods to sea-ice motion in Antarctica. Proc. SPIE. 2003; 5155:249–256. DOI: 10.1117/12.506209
60. Isleifson D, Langlois A, Barber DG, Shafai L. C-Band scatterometer measurements of multiyear sea ice before fall freeze-up in the Canadian Arctic. IEEE Trans. Geosci. Remote Sens. Jun; 2009 47(6):1651–1661. DOI: 10.1109/TGRS.2008.2006566
61. Lindell DB, Long DG. Multiyear Arctic ice classification using ASCAT and SSMIS. Remote Sens. Mar.2016 8 art. 204. doi: 10.3390/rs8040294
62. Swan AM, Long DG. Multi-year Arctic sea ice classification using QuikSCAT. IEEE Trans. Geosci. Remote Sens. Sep; 2012 50(9):3317–3326. DOI: 10.1109/TGRS.2012.2184123
63. Lindell DB, Long DG. Multiyear Arctic sea ice classification using OSCAT and QuikSCAT. IEEE Trans. Geosci. Remote Sens. Jan; 2016 54(1):167–175. DOI: 10.1109/TGRS.2015.2452215
64. Lecomte P, Cavanie A, Gohin F. Recognition of sea ice zones using ERS-1 scatterometer data. Proc. Int. Geosci. Remote Sens. Symp. 1993:855–857.
65. Remund QP, Long DG, Drinkwater MR. An iterative approach to multisensor sea ice classification. IEEE Trans. Geosci. Remote Sens. Jul; 2000 38(4):1843–1856. DOI: 10.1109/36.851768
66. Voss S, Heygster G, Ezraty R. Improving sea ice type discrimination by the simultaneous use of SSM/I and scatterometer data. Polar Res. 2006; 22(1):25–42. DOI: 10.1111/j.1751-8369.2003.tb00093.x
67. Walker NP, Partington KC, Van Woert ML, Street TLT. Arctic sea ice type and concentration mapping using passive and active microwave sensors. IEEE Trans. Geosci. Remote Sens. Dec; 2006 44(12):3574–3584.
68. Tonboe R, Toudal L. Classification of new-ice in the Greenland Sea using satellite SSM/I radiometer and SeaWinds scatterometer data and comparison with ice model. Remote Sens. Environ. 2005; 97(3):277–287.
69. Swift CT. Seasat scatterometer observations of sea ice. IEEE Trans. Geosci. Remote Sens. Mar; 1999 37(2):716–723.
70. Kwok R. Sea ice convergence along the Arctic coasts of Greenland and the Canadian Arctic Archipelago: Variability and extremes (1992– 2014). Geophys. Res. Lett. 2015; 42(18):7598–7605.

71. Nghiem SV, et al. Depletion of perennial sea ice in the East Arctic Ocean. *Geophys. Res. Lett.* 2006; 33 Art. no. L17501. doi: 10.1029/2006GL027198
72. Nghiem SV, Rigor IG, Perovich DK, Clemente-Colon P, Weatherly JW, Neumann G. Rapid reduction of Arctic perennial sea ice. *Geophys. Res. Lett.* 2007; 34 Art. no. L19504. doi: 10.1029/2007GL031138
73. Zygmuntowska I M, Rampal P, Ivanova N, Smedsrud LH. Uncertainties in Arctic sea ice thickness and volume: New estimates and implications for trends. *Cryosphere.* 2014; 8:705–720.
74. Carsey FD. Summer arctic sea ice character from satellite microwave data. *J. Geophys. Res.* 1985; 90(C3):5015–5034.
75. Howell SEL, Tivy A, Yackel JJ, Scharien RK. Application of a SeaWinds/QuikSCAT sea ice melt algorithm for assessing melt dynamics in the Canadian Arctic Archipelago. *J. Geophys. Res.* 2006; 111 Art. no. C07025. doi: 10.1029/2005JC003193
76. Hallikainen M, Sieviene P, Zhang Y, Halme P. Use of QuikSCAT Ku-band scatterometer data for retrieval of seasonal snow characteristics in Finland. *Proc. IEEE Int. Geosci. Remote Sens. Symp.* Sep 23–28.2007 :1228–1228. DOI: 10.1109/IGARSS.2007.4423027
77. Drinkwater MR, Liu X. Seasonal to interannual variability in Antarctic sea-ice surface melt. *IEEE Trans. Geosci. Remote Sens.* Jul; 2000 38(4):1827–1842.
78. Forster RR, Long DG, Jezek KC, Drobot SD, Anderson MR. The onset of Arctic sea-ice snowmelt as detected with passive-and active-microwave remote sensing. *Ann. Glaciology.* 2001; 33(1):85–93. DOI: 10.3189/172756401781818428
79. Mortin J, et al. Extending the QuikSCAT record of seasonal melt-freeze transitions over Arctic sea ice using ASCAT. *Remote Sens. Environ.* 2014; 141:214–230. DOI: 10.1016/j.rse.2013.11.004
80. Howell SEL, Brown LC, Kang K-K, Duguay CR. Variability in ice phenology on Great Bear Lake and Great Slave Lake, Northwest Territories, Canada, from SeaWinds/QuikSCAT: 2000–2006. *Remote Sens. Environ.* 2008; 113(4):816–834. DOI: 10.1016/j.rse.2008.12.007
81. Howell SEL, Assini J, Young KL, Abnizova A, Derksen C. Snowmelt variability in Polar Bear Pass, Nunavut, Canada, from QuikSCAT: 2000–2009. *Hydrological Processes.* 2012; 26(23): 2477–3488. DOI: 10.1002/hyp.8365
82. Nghiem SV, Tsai W-Y. Global snow cover monitoring with spaceborne Ku-band scatterometer. *IEEE Trans. Geosci. Remote Sens.* Oct; 2001 38(10):2118–2134.
83. Jezek KC, Gogineni P, Shanableh M. Radar measurements of zones on the Greenland ice sheet. *Geophys. Res. Lett.* 1994; 21(1):33–36.
84. Ashcraft IS, Long DG. Observation and characterization of radar backscatter over Greenland. *IEEE Trans. Geosci. Remote Sens.* Feb; 2005 43(2):237–246. DOI: 10.1109/TGRS.2004.825588
85. Drinkwater MR, Long DG, Bingham AW. Greenland snow accumulation estimates from scatterometer data. *J. Geophys. Res.* 2001; 106(D24):33935–33950. DOI: 10.1029/2001JD900107
86. Dierking W, Linow S, Rack W. Toward a robust retrieval of snow accumulation over the Antarctic ice sheet using satellite radar. *J. Geophys. Res.* 2012; 117(D9)doi: 10.1029/2011JD017227
87. Nghiem, SV., Steffen, K., Huff, R., Neumann, G. Snow accumulation and snowmelt monitoring in Greenland and Antarctica. In: Tregoning, P., Rizos, C., editors. *Dynamic Planet.* Berlin, Germany: Springer-Verlag; 2007. p. 31-38.ch. 5
88. Benson CS. Stratigraphic studies in the snow and firn of the Greenland ice sheet. *Snow, Ice Permafrost Res. Establishment Res. Rep.* 1962; (70)
89. Winebrenner, DP., Long, DG., Holt, B. Automatable observation of seasonal transitions on Arctic sea ice using synthetic aperture radar. In: Tsatsoulis, C., Kwok, R., editors. *Recent Advances in the Analysis of SAR for Studies in the Polar Oceans.* Berlin, Germany: Springer-Verlage; 1998. p. 129-144.
90. Ashcraft IS, Long DG. Relating microwave backscatter azimuth modulation to surface properties of the Greenland Ice Sheet. *J. Glaciology.* 2006; 52(177):257–266.
91. Ashcraft IS, Long DG. Comparison of methods for melt detection over Greenland using active and passive microwave measurements. *Int. J. Remote Sens.* 2006; 27(12):2569–2488.
92. Barrand NE, et al. Trends in Antarctic Peninsula surface melting conditions from observations and regional climate modeling. *J. Geophys. Res.: Earth Surf.* 2013; 118(1):315–330. DOI: 10.1029/2012JF002559

93. Hicks BR, Long DG. Inferring Greenland melt and refreeze severity from SeaWinds scatterometer data. *Int. J. Remote Sens.* 2011; 32(23):8053–8080. DOI: 10.1080/01431161.2010.532174
94. Ledroit M, Remy F, Minster J-F. Observations of the Antarctic ice sheet with the Seasat scatterometer: Relation to katabatic-wind intensity and direction. *J. Glaciology.* 1993; 39(132): 385–394.
95. Long DG, Drinkwater MR. Azimuth variation in microwave scatterometer and radiometer data over Antarctica. *IEEE Trans. Geosci. Remote Sens.* Jul; 2000 38(4):1857–1870.
96. Fraser AD, Young NW, Adams N. Comparison of microwave backscatter anisotropy parameterizations of the Antarctic ice sheet using ASCAT. *IEEE Trans. Geosci. Remote Sens.* Mar; 2014 52(3):1583–1595.
97. Lindsley R, Long DG. ASCAT and QuikSCAT azimuth modulation of backscatter over East Antarctica. *IEEE Trans. Geosci. Remote Sens.* Aug; 2016 13(8):1134–1138.
98. Scambos TA, et al. Extent of low-accumulation ‘wind glaze’ areas on the East Antarctic Plateau: Implications for continental ice mass balance. *J. Glaciology.* 2012; 58(210):633–647. DOI: 10.3189/2012JoG11j232
99. Moon KR, Long DG. Considerations for Ku-band scatterometer calibration using the dry snow zone of the Greenland ice sheet. *IEEE Trans. Geosci. Remote Sens.* Nov; 2013 10(6):1344–1349. DOI: 10.1109/LGRS.2013.2241012
100. Nghiem SV, et al. The extreme melt across the Greenland ice sheet in 2012. *Geophys. Res. Lett.* 2012; 39(20) Art. no. L20502. doi: 10.1029/2012GL053611
101. Williams RS Jr, Hall DK, Benson CS. Analysis of glacier facies using satellite techniques. *J. Glaciology.* 1991; 37(125):120–128.
102. Nghiem SV, Steffen K, Kwok R, Tsai W-Y. Detection of snowmelt regions on the Greenland ice sheet using diurnal backscatter change. *J. Glaciology.* 2001; 47(159):539–547.
103. Bingham AW, Drinkwater MR. Recent changes in the microwave scattering properties of the Antarctic ice sheet. *IEEE Trans. Geosci. Remote Sens.* Jul; 2000 38(4):1810–1820.
104. Bhattacharya I, Jezek KC, Wang L, Liu H. Surface melt area variability of the Greenland ice sheet: 1979–2008. *Geophys. Res. Lett.* 2009; 36(20) Art. no. L20502. doi: 10.1029/2009GL039798
105. Wang L, Sharp M, Rivard B, Steffen K. Melt season duration and ice layer formation on the Greenland Ice Sheet, 2000–2004. *J. Geophys. Res.* 2007; 112 no. F04013. doi: 10.1029/2007JF000760
106. Wismann V. Monitoring of seasonal snowmelt on Greenland with ERS scatterometer data. *IEEE Trans. Geosci. Remote Sens.* Jul; 2000 38(4):1821–1826.
107. Trusel LD, Frey KE, Das SB. Antarctic surface melting dynamics: Enhanced perspectives from radar scatterometer data. *J. Geophys. Res.: Earth Surf.* 2012; 117(F2) Art. no. F02002. doi: 10.1029/2011JF002126
108. Rotschky G, Schuler TV, Haarpainter J, Kohler J, Isaksson E. Spatio-temporal variability of snowmelt across Svalbard during the period 2000–08 derived from QuikSCAT/SeaWinds scatterometry. *Polar Res.* 2011; 30 Art. no. 5963. doi: 10.3402/polar.v30i0.5963
109. Wang L, Sharp MJ, Rivard B, Marshall S, Burgess D. Melt season duration on Canadian Arctic Ice Caps, 2000–2004. *Geophys. Res. Lett.* 2005; 32 Art. no. L19502. doi: 10.029/2005GL023962
110. Nghiem SV, Steffen K, Kwok R, Tsai W-Y. Detection of snowmelt regions on the Greenland ice sheet using diurnal backscatter change. *J. Glaciology.* 2002; 47(159):539–547.
111. Scambos, T., Hulbe, C., Fahnestock, M. Climate-induced ice shelf disintegration in the Antarctic Peninsula. In: Domack, E., et al., editors. *Antarctic Peninsula Climate Variability: Historical and Paleoenvironmental Perspectives*, (Antarct. Res. Ser.). Vol. 79. Washington, D.C., USA: American Geophysical Union; 2003. p. 79–92.
112. Kunz LB, Long DG. Melt detection in Antarctic iceshelves using spaceborne scatterometers and radiometers. *IEEE Trans. Geosci. Remote Sens.* Sep; 2006 44(9):2461–2469. DOI: 10.1109/TGRS.2006.874138
113. Pritchard HD, Ligtenberg SRM, Fricker HA, Vaughan DG, van den Broeke MR, Padman L. Antarctic ice-sheet loss driven by basal melting of ice shelves. *Nature.* 2012; 484:502–505. [PubMed: 22538614]

114. Alley KE, Scambos TA, Siegfried MR, Fricker HA. Impacts of warm water on Antarctic ice shelf stability through basal channel formation. *Nature Geosci.* 2016; 9:290–293. DOI: 10.1038/ngeo2675
115. Vernet M, et al. Islands of ice: Influence of free-drifting Antarctic icebergs on pelagic marine ecosystems. *Oceanography.* 2012; 25(3):38–39. DOI: 10.5670/oceanog.2012.72
116. Smith KL, Sherman AD, Shaw TJ, Sprintall J. Icebergs as unique Lagrangian ecosystems in polar seas. *Mar. Sci.* 2013; 5:269–287. DOI: 10.1146/annurev-marine-121211-172317
117. Scambos T, et al. Calving and ice-shelf break-up processes investigated by proxy: Antarctic tabular iceberg evolution during northward drift. *J. Glaciology.* 2008; 54(187):579–591.
118. Stuart KM, Long DG. Tracking large tabular icebergs using the SeaWinds Ku-band microwave scatterometer. *Deep-Sea Res. Part II.* 2011; 58:1285–1300. DOI: 10.1016/j.dsr2.2010.11.004
119. Stuart KM, Long DG. Iceberg size and orientation estimation using SeaWinds. *Cold Regions Sci. Technol.* 2011; 69:39–51. DOI: 10.1016/j.coldregions.2011.07.006
120. Stephen H, Long DG. Study of iceberg B10A using scatterometer data. *Proc. IEEE Int. Geosci. Remote Sens. Symp.* 2000; 3:1340–1342.
121. Tournadre J, Bouhier N, Girard-Ardhuin F, Remy F. Large iceberg characteristics from altimeter waveforms analysis. *J. Geophys. Res.: Oceans.* 2015; 120:1954–1974. DOI: 10.1002/2014JC010402
122. Evers LG, Green DN, Young NW, Snellen M. Remote hydroacoustic sensing of large icebergs in the southern Indian Ocean: Implications for iceberg monitoring. *Geophys. Res. Lett.* 2014; 40(17):4694–4699. DOI: 10.1002/grl.50914
123. Talandier J, Hyvernaud O, Reymond D, Okal EA. Hydroacoustic signals generated by parked and drifting icebergs in the Southern Indian and Pacific Oceans. *Geophys. J. Int.* 2006; 165:817–834. DOI: 10.1111/j.1365-246X.2006.02911.x
124. Matsumoto H, et al. Antarctic icebergs: A significant natural ocean sound source in the Southern Hemisphere. *Geochem., Geophys., Geosystems.* 2014; 15(8):3448–3458. DOI: 10.1002/2014GC005454
125. Long DG, Ballantyne J, Bertoia C. Is the number of icebergs really increasing? *EOS, Trans. Amer. Geophys. Union.* Oct 15; 2002 83(42):469–474.
126. Center for Ocean-Atmospheric Prediction Studies. [Accessed on: Oct. 2016] Scatterometry & Ocean Vector Winds. 2016. [Online]. Available: <http://coaps.fsu.edu/scatterometry/about/overview.php>
127. Fois F, Hoogeboom P, Le Chevalier F, Stofflen A. Future ocean scatterometry: On the use of cross-polar scattering to observe very high winds. *IEEE Trans. Geosci. Remote Sens. Sep; 2015* 43(9):5009–5020.

Biography



David G. Long (S'80–SM'98–F'08) received the Ph.D. degree in electrical engineering from the University of Southern California, Los Angeles, CA, USA, in 1989.

From 1983 to 1990, he worked for NASA's Jet Propulsion Laboratory (JPL), where he developed advanced radar remote sensing systems. While at JPL, he was the Project Engineer on the NASA Scatterometer project that flew from 1996 to 1997. He also managed

the SCANSAT project, the precursor to SeaWinds that was flown in 1999 on QuikSCAT, in 2002 on ADEOS-II, and as RapidScat in 2014 on the International Space Station. He is currently a Professor in the Electrical and Computer Engineering Department, Brigham Young University, Provo, UT, USA, where he teaches upper division and graduate courses in communications, microwave remote sensing, radar, and signal processing and is the Director of the BYU Center for Remote Sensing, Provo. He is the Principal Investigator on several NASA-sponsored research projects in remote sensing. He has more than 400 publications in various areas including signal processing, radar scatterometry, and synthetic aperture radar. His research interests include microwave remote sensing, radar theory, space-based sensing, estimation theory, signal processing, and mesoscale atmospheric dynamics.

Dr. Long has received the NASA Certificate of Recognition several times and is an Associate Editor for the IEEE GEOSCIENCE AND REMOTE SENSING LETTERS.

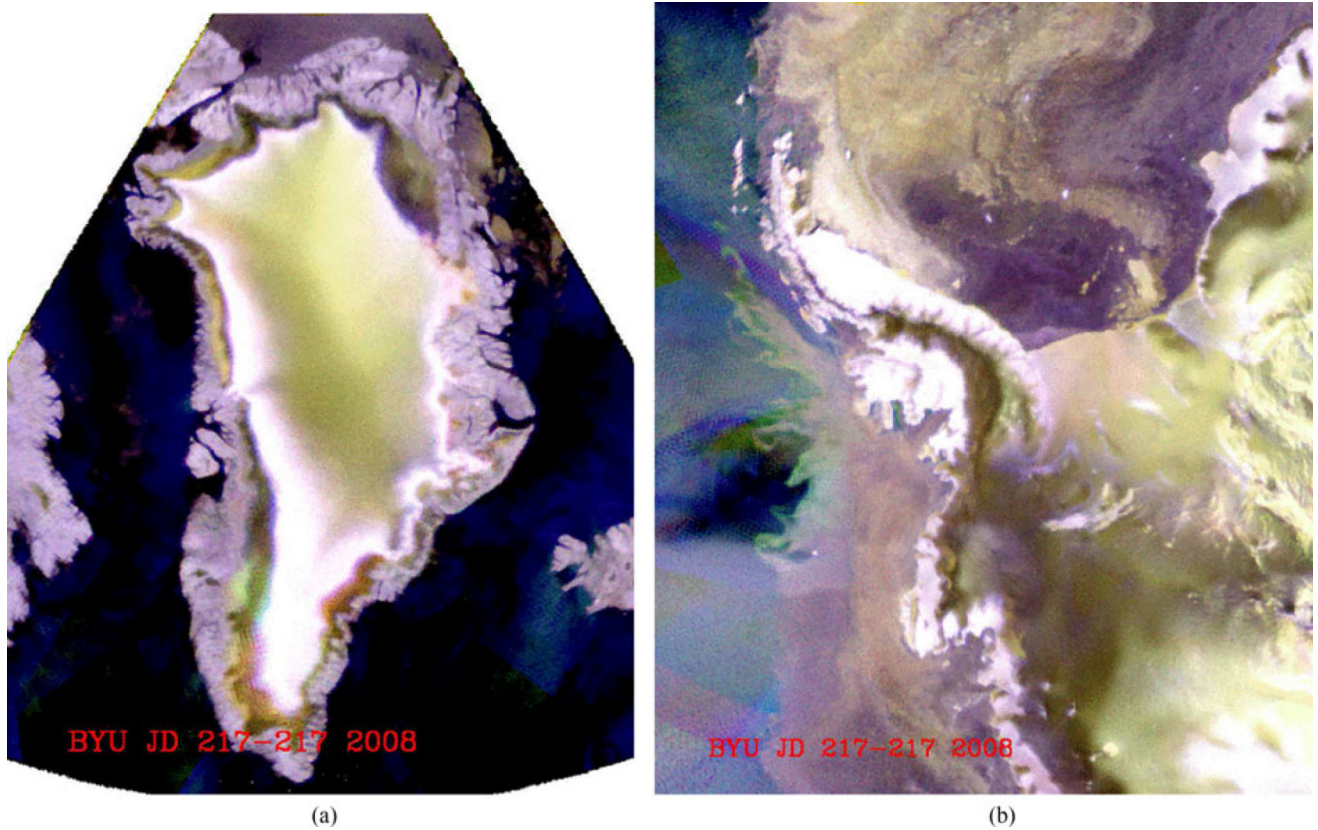


Fig. 1.

False color, enhanced-resolution backscatter images of Greenland and western Antarctica created from QuikSCAT and ASCAT data for day 217, 2008. Red is Ku-band HH-pol σ^0 , green is Ku-band VV-pol σ^0 , and blue is C-band VV-pol σ^0 . (a) Greenland. Bare land tends to appear purple, while the dry snow zone appears in shades of gold that are related to the local accumulation. White, which has the highest backscatter, delineates the frozen wet snow zone. The dark band surrounding the white central area is indicative of melt conditions in the saturated snow and bare ice zones. (b) Antarctica. Green and blue correspond to open ocean, which appears stippled due to changes in wind condition during the day. Small icebergs appear white against the purple and gold sea ice, where the colors correspond to new and multiyear sea ice, respectively. Glaciated regions over land are gold colored with some icebergs in gold in the upper right quadrant of the image. High backscatter regions that appear white correspond to ice and show that has partially melted and refrozen. On the left side tendrils of sea ice extend into the ocean just below the curving Antarctic Peninsula.

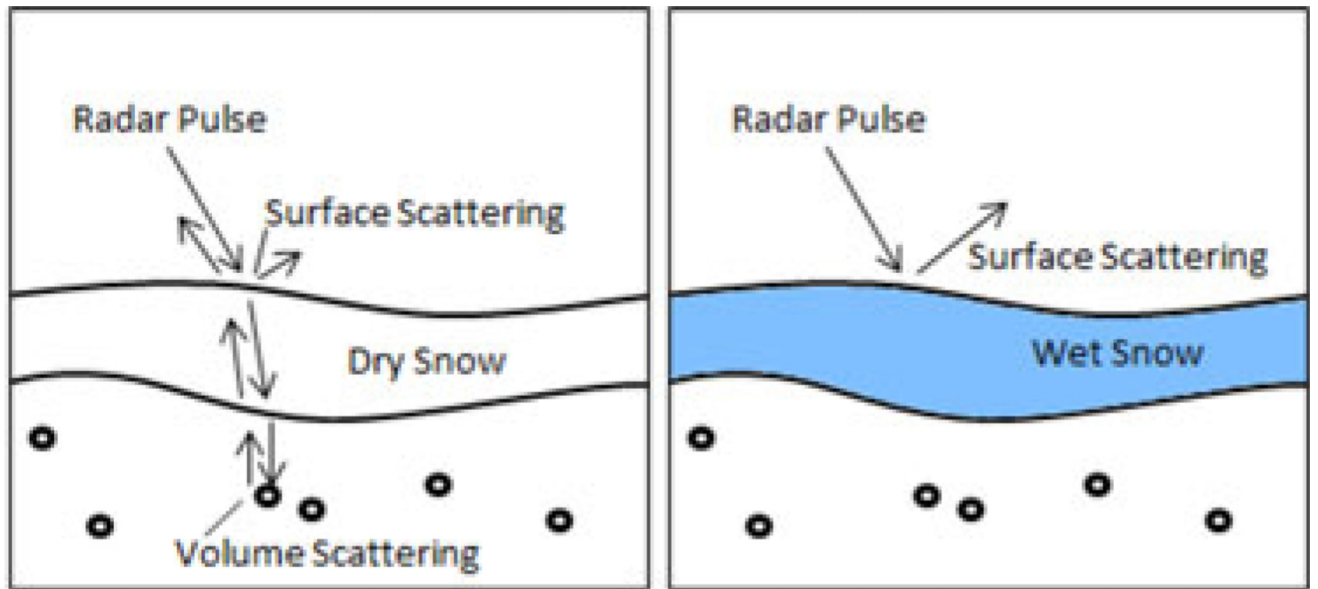


Fig. 2.
Illustration of the impact of surface melt on the backscattering mechanism in snow layers.

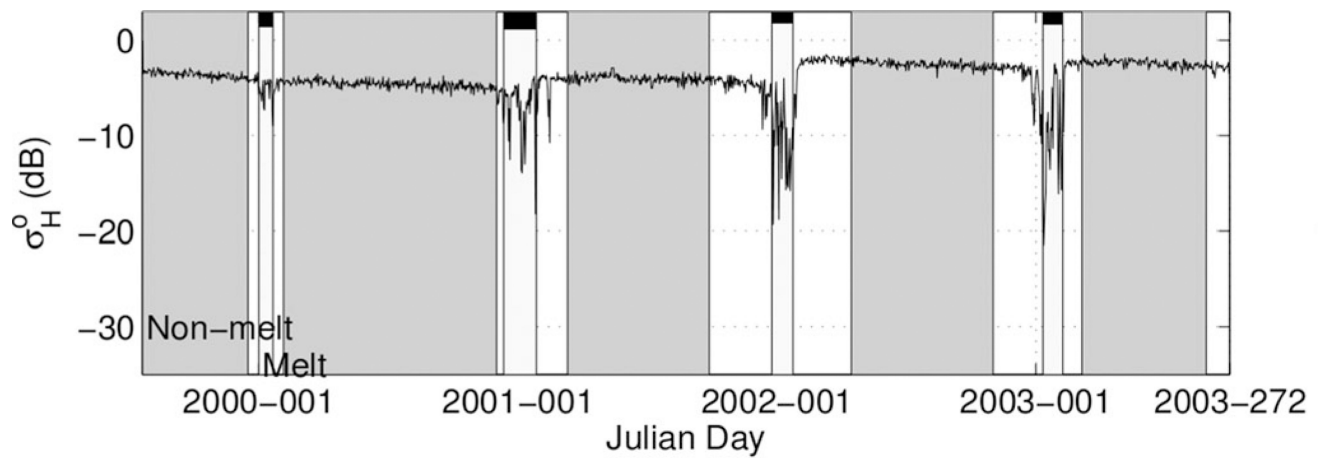


Fig. 3.

Time series of daily-averaged Ku-band HH σ^o versus time for a point near the terminus of the Amery ice Shelf in Antarctica illustrating the impact of melt on glacial scattering. See text. Vertical narrow bands topped with black bars denote periods of high variability backscatter that correspond to melt periods. Gray bands are midwinter periods used for calibrating the backscatter variability. White bands are transition periods.

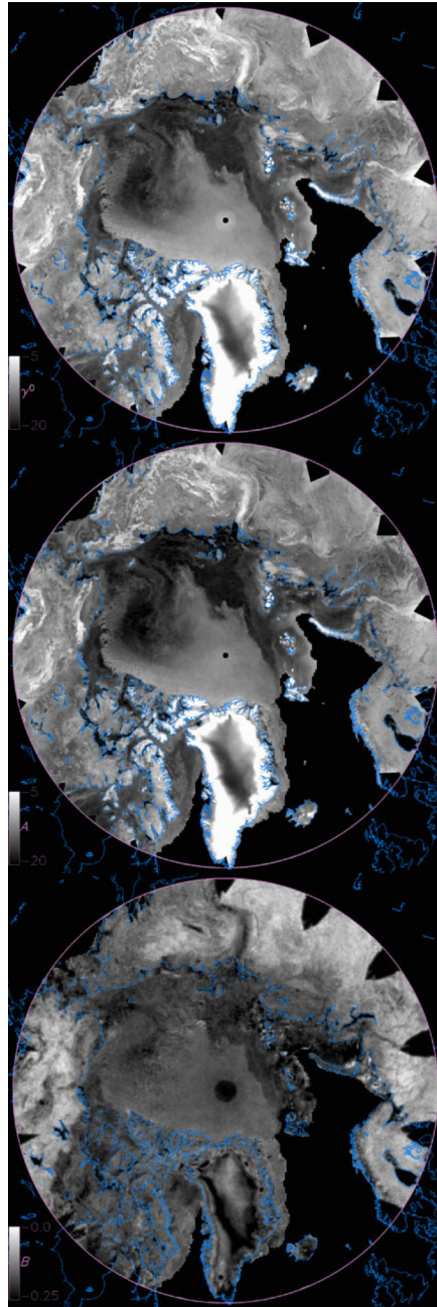


Fig. 4.

ASCAT C-band VV view of the Northern Hemisphere for days 10–11 (midwinter) of 2010.

(top) γ_{dB}^O , (center) \mathcal{A} , (bottom) B . Open ocean has been masked off. Black triangular areas around the perimeter of this polar stereographic projection are areas not covered by the scatterometer in the two-day imaging period used.

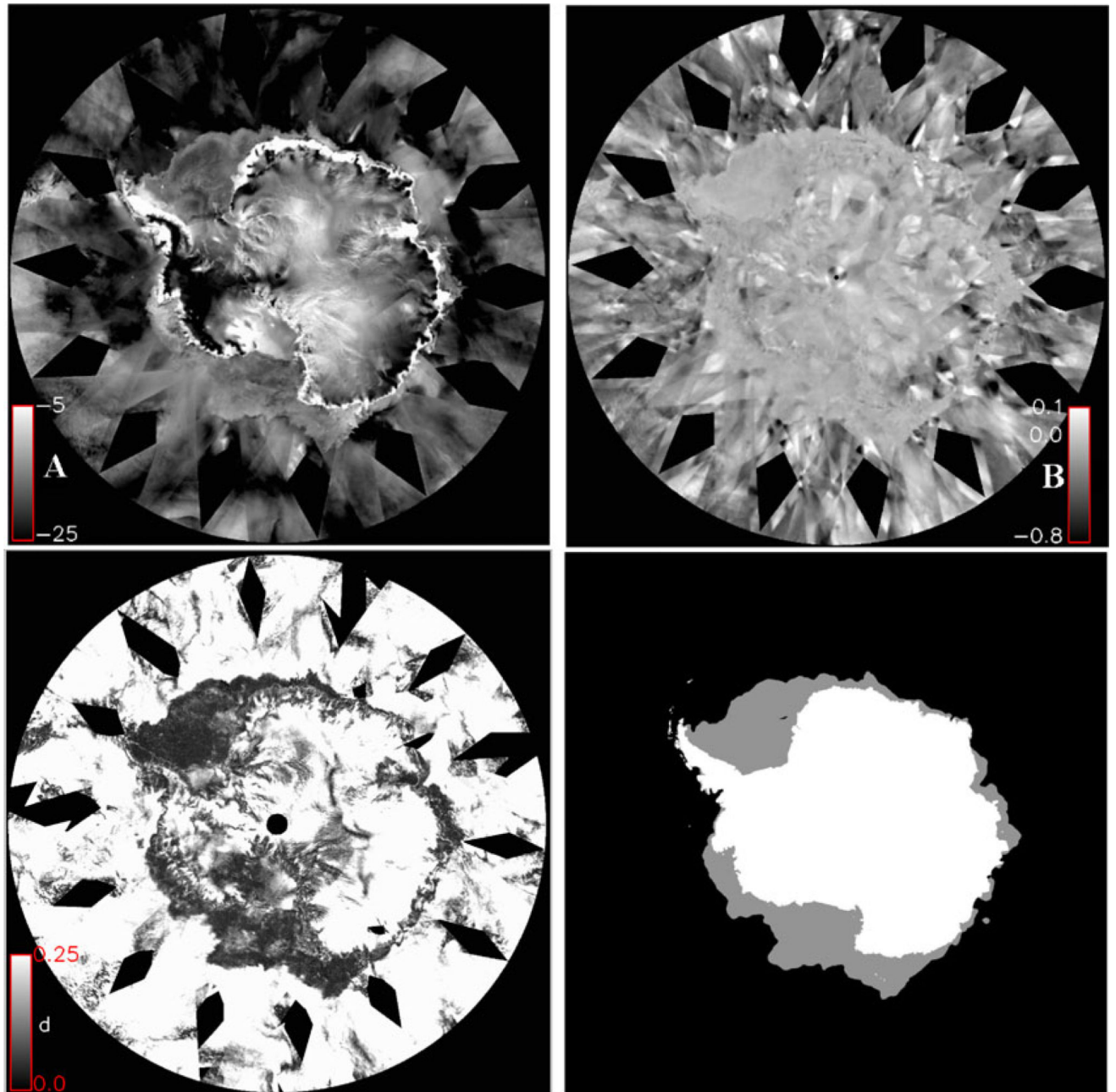
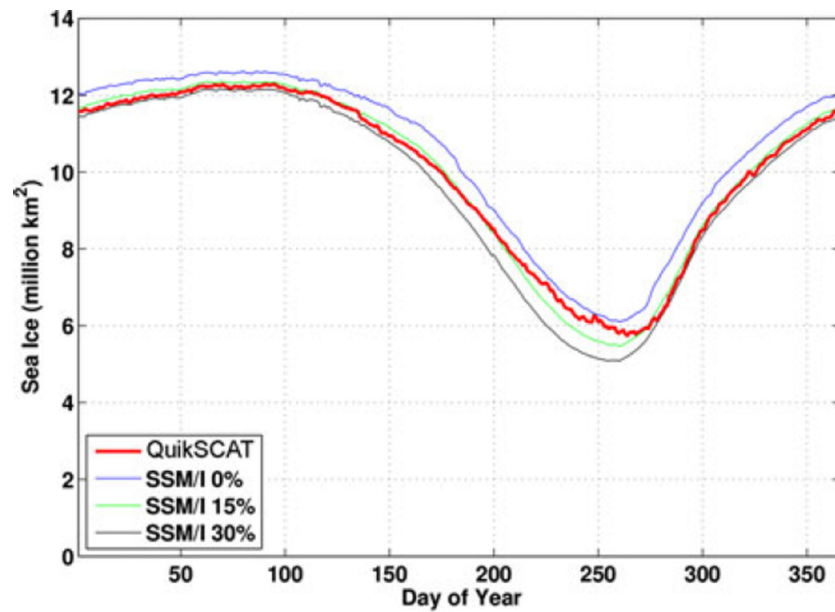
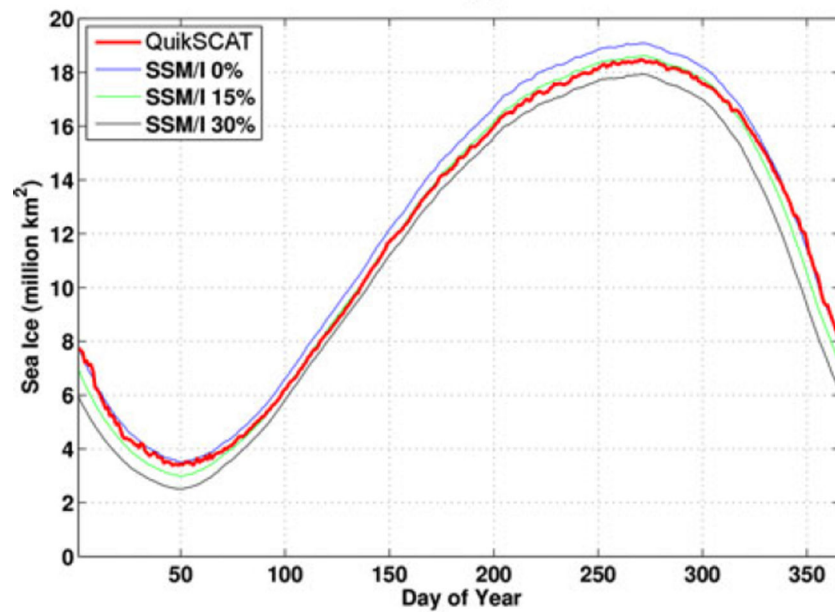


Fig. 5. ASCAT images for day 80, 2009. (upper left) \mathcal{A} , (upper right) \mathcal{B} , (lower left) d , (lower right) sea-ice mask.



(a)



(b)

Fig. 6. Mission-averaged (1999–2009) daily sea-ice area for the (a) Arctic (above 60°) and (b) Antarctic derived from QuikSCAT data by using the Remund–Long algorithm [36] compared to ice area computed from SSM/I sea-ice concentration derived by using the NASA Team algorithm [52], [53] for the same period. Each line SSM/I lines show the area within the percent sea-ice contour.

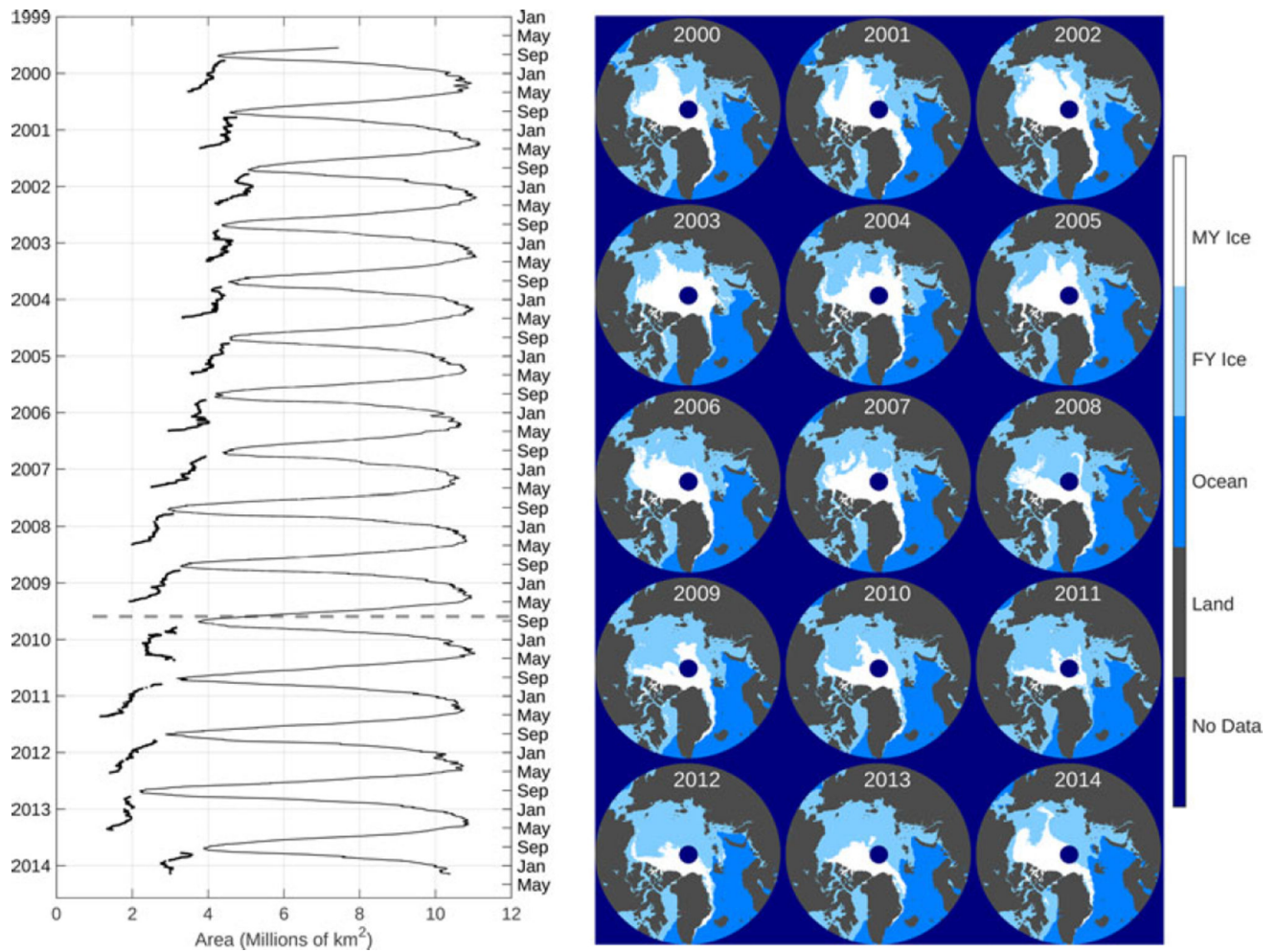


Fig. 7.

QuikSCAT and OSCAT ice classification results for the Arctic above 65° N. (left panel) FY ice (thin line) and MY ice (thick line). During the late summer ice classification is not done, resulting in gaps in the MY ice line [63]. The dashed line is the division between QuikSCAT and OSCAT. (right panel) Maps of FY and MY ice for day 45 of years 2002–2014 [63].

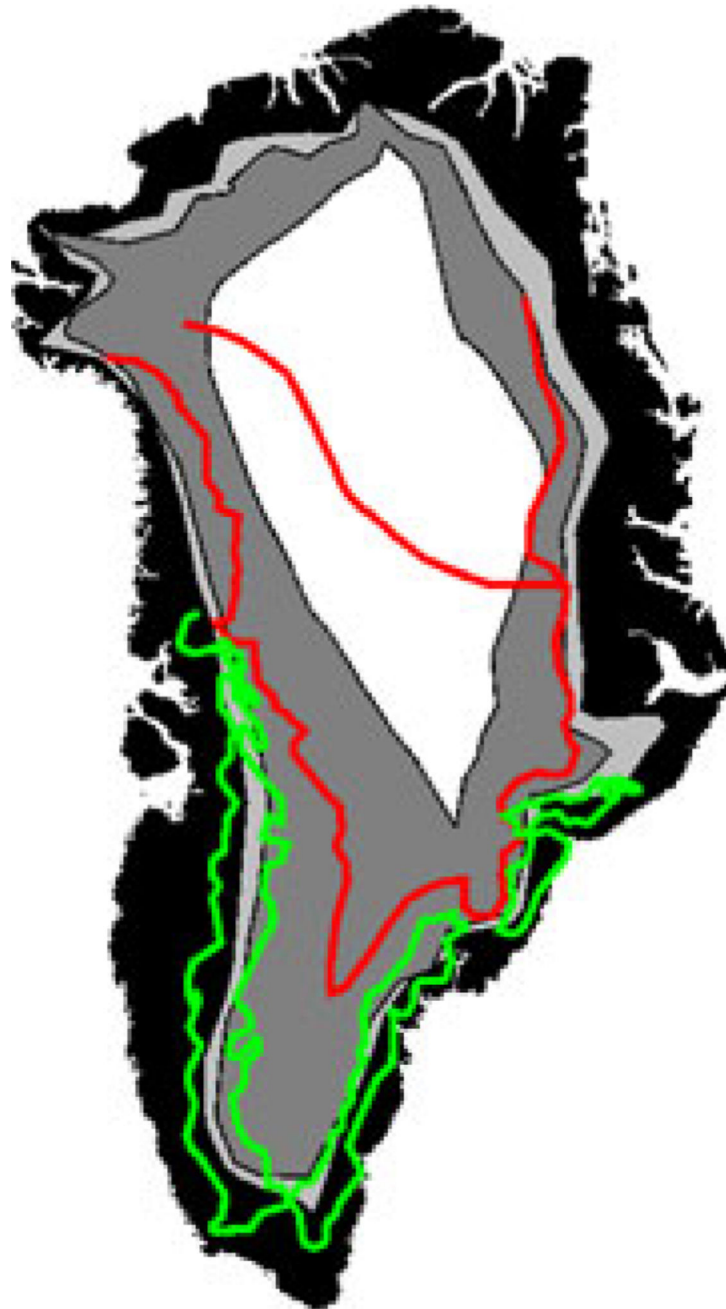


Fig. 8.

Greenland facies map. Shaded areas are the facies from Benson [88], where the central white is dry snow, dark gray is the percolation zone, and light gray is the saturated snow zone. Colored lines are zones derived from 1978 SASS data [38] that only extend to 78° N. Red denotes the dry snow zone with two accumulation divisions. Green outlines the saturated zone.

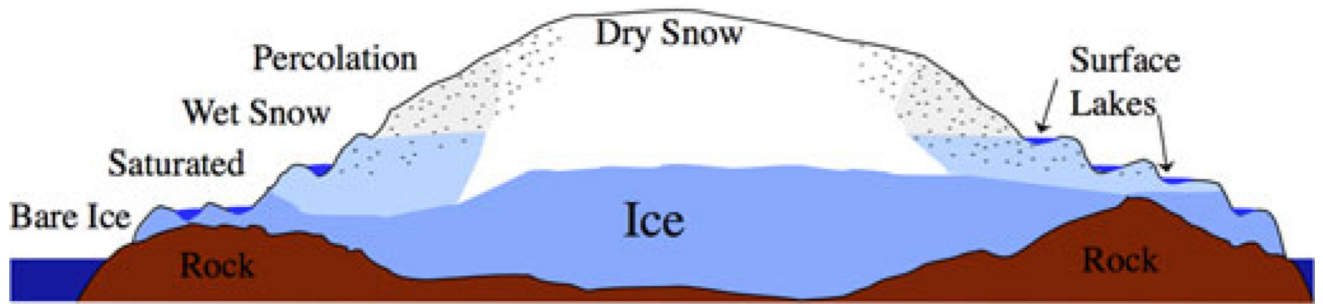


Fig. 9.
Greenland facies illustration showing a schematic meridional section or slice through the Greenland ice sheet.

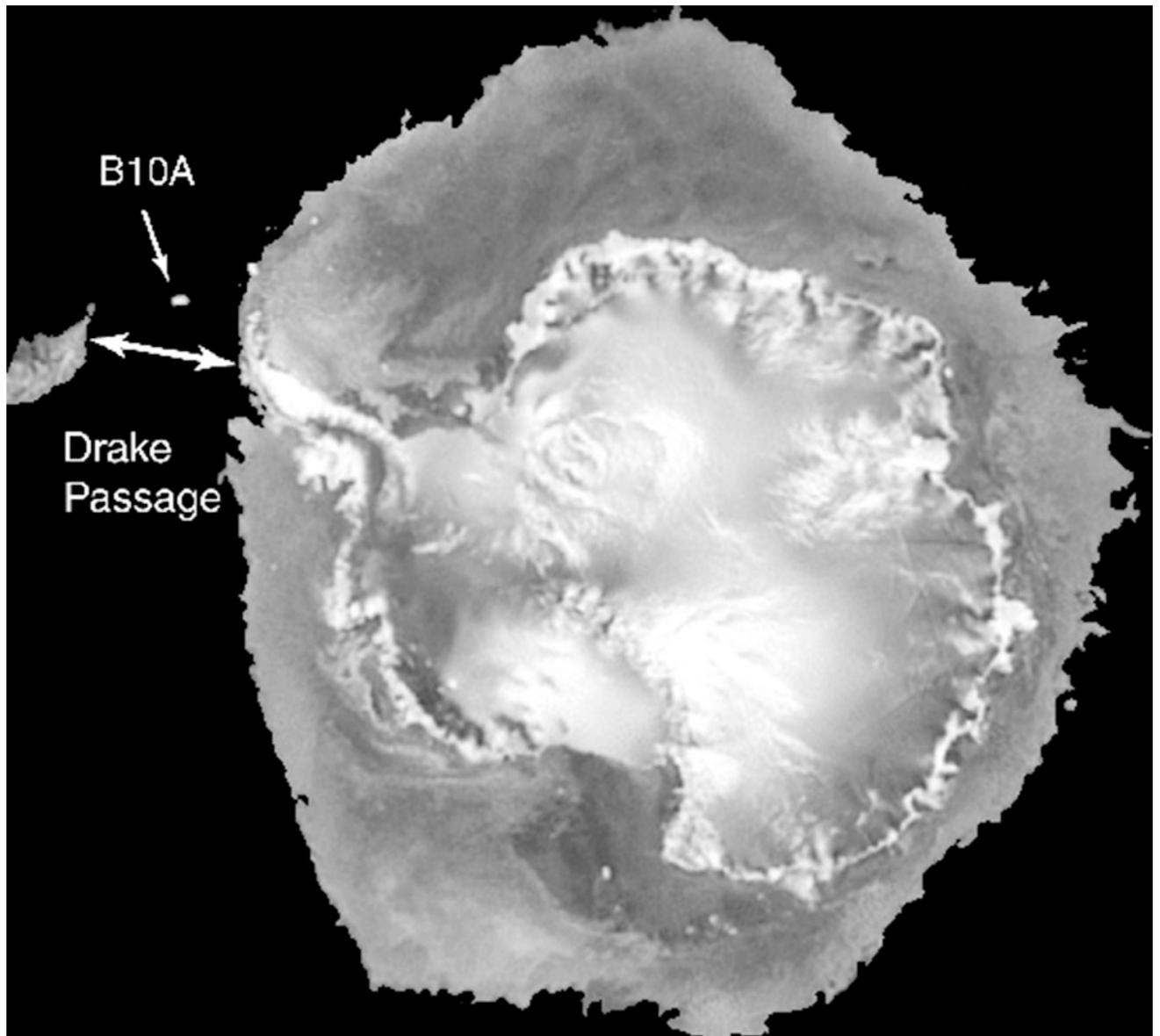


Fig. 10.

First QuikSCAT HH σ^0 image of Antarctica. Iceberg B10A is visible as the white area in the Drake Passage between the southern tip of South America and the northern extent of the Antarctic Peninsula in the upper left of this image. Open ocean has been set to black in this image. Line features in the lower right of the continent are imaging artifacts resulting from the strong azimuth modulation of σ^0 in this area due to sastrugi [95].

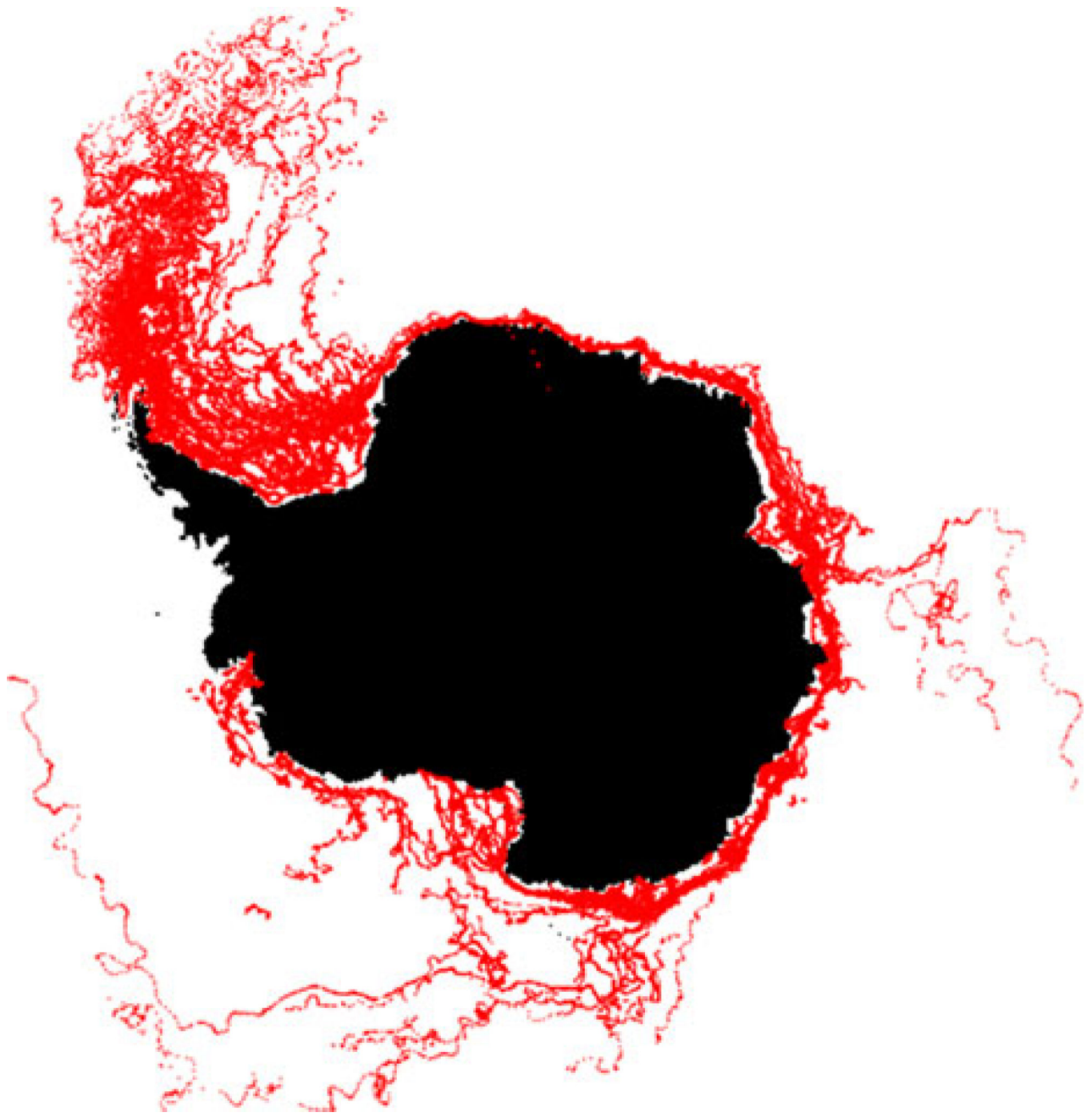


Fig. 11.

Plotted daily positions of well over 100 Antarctic tabular icebergs derived from scatterometer data spanning 1978–2016 from the Scatterometer Climate Record Pathfinder (www.scp.byu.edu). Due to the strong counterclockwise transport of icebergs from the Ross Sea (at the bottom) around the Antarctic continent (black) near the coast, more than 95% of all Antarctic icebergs are transported through the Weddell Sea (at the upper left of the image)—regardless of their origin [118].

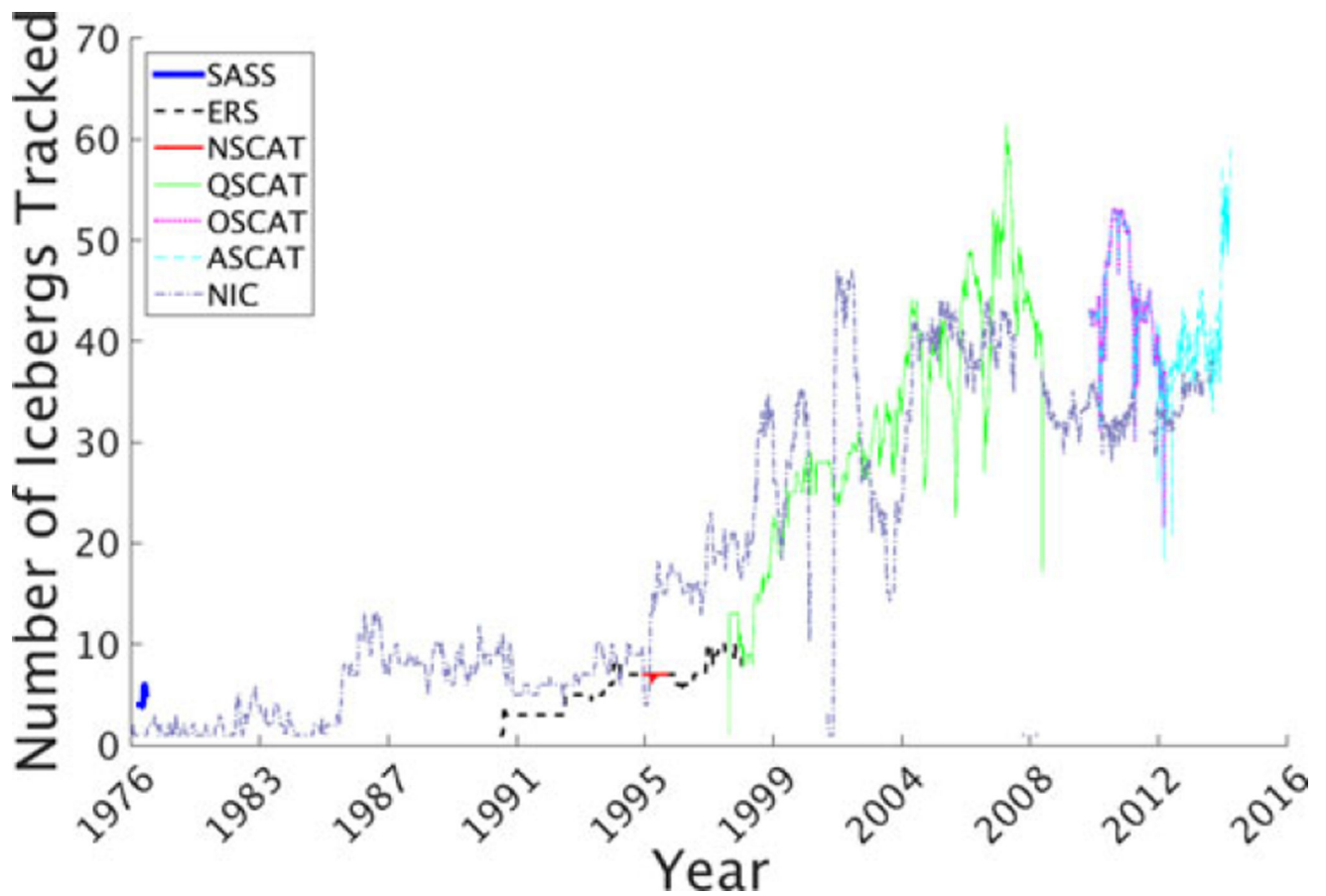

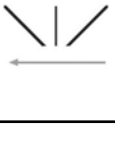


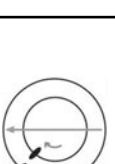

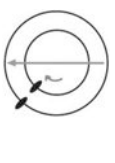
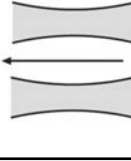

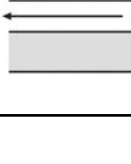
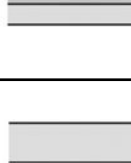





Fig. 12.

Plot of the number of Antarctic icebergs being tracked by the U.S. NIC and by researchers using scatterometer data from 1978 to June 2016. The various scatterometers in the legend are the U.S. SASS [1978], the ERS-1 and ERS-2 scatterometers [1992–2000], the NSCAT [1996–1997], the QuikSCAT scatterometer [1999–present], the OceanSat-2 scatterometer OSCAT [2009–2000], and the ASCAT [2008–present].

TABLE I

Historic and Current Wind Scatterometers

	SASS	ESCAT	NSCAT	Sea Winds	ASCAT	OSCAT	HY-2A
Frequency & Band	14.6 GHz (Ku)	5.3 GHz (C)	13.995 GHz (Ku)	13.4 GHz (Ku)	5.3 GHz (C)	13.515 GHz (Ku)	13.255 GHz (Ku)
Antenna Configuration							
Polarization	VV and HH	VV	W, VV & HH, W	W-outer / HH-inner	VV	W-outer/ HH-inner	W-outer/HH-inner
Beam Resolution	Fixed Doppler	Range gate	Variable Doppler	Pencil-beam	Range gate	Pencil-beam	Pencil-beam
Resolution (σ°)	nominally 50 km	50 km	25 km	Egg: 25×35 km Slice: 6×25 km	SZO: 25/50 km SZF: 4×20 km	Egg: 30×68 km Slice: 6×30 km	Inner: 23×33 km Outer: 26×37 km
Swath Configuration & Width in km							
Incidence Angles	0° – 70°	18° – 59°	17° – 60°	46° & 54.4°	25° – 65°	49° & 57°	41° & 48°
Mission & Dates	SEASAT: 6/78-10/78	ERS-1:7/91-3/0C ERS-2:4/95-5/11	ADEOS-I: 8/96-6/97	QuikSCAT: 6/99-11/09* ADEOS-II: 1/02-10/02 RapidScat: 10/14-8/16	METOP-A: 6/07- METOP-B: 9/12-	OceanSat-2:10/09-2/14 ScatSat-1:8/16-	HY-2A:8/11-

* continues operation in non-spinning mode